Inorganic Chemistry

Article

Cite This: Inorg. Chem. 2017, 56, 14023-14039

pubs.acs.org/IC

A_2MnXO_4 Family (A = Li, Na, Ag; X = Si, Ge): Structural and Magnetic Properties

Vladimir B. Nalbandyan,*[,†] Elena A. Zvereva,[‡,§] Igor L. Shukaev,[†] Elijah Gordon,[∥] Vladimir V. Politaev,[†] Myung-Hwan Whangbo,[∥] Aleksandr A. Petrenko,[†] Roman S. Denisov,[‡] Maria M. Markina,[‡] Michael Tzschoppe,[⊥] Kirill Yu. Bukhteev,[‡] Rüdiger Klingeler,[⊥,#] and Alexander N. Vasiliev[‡,§,¶]

[†]Chemistry Faculty, Southern Federal University, Rostov-on-Don 344090, Russia

[‡]Faculty of Physics, Moscow State University, Moscow 119991, Russia

[§]National Research South Ural State University, Chelyabinsk 454080, Russia

[∥]Department of Chemistry, North Carolina State University, Raleigh, North Carolina 27695-8204, United States

[⊥]Kirchhoff Institute for Physics, INF 227, Heidelberg University, D-69120 Heidelberg, Germany

[#]Centre for Advanced Materials (CAM), INF 225, Heidelberg University, D-69120 Heidelberg, Germany

[¶]National University of Science and Technology "MISiS", Moscow 119049, Russia

Supporting Information

ABSTRACT: Four new manganese germanates and silicates, A_2MnGeO_4 (A = Li, Na) and A_2MnSiO_4 (A = Na, Ag), were prepared, and their crystal structures were determined using the X-ray Rietveld method. All of them contain all components in tetrahedral coordination. Li_2MnGeO_4 is orthorhombic ($Pmn2_1$) layered, isostructural with Li_2CdGeO_4, and the three other compounds are monoclinic (Pn) cristobalite-related frameworks. As in other stuffed cristobalites of various symmetry (Pn A_2MXO_4, $Pna2_1$ and $Pbca$ AMO_2), average bond angles on bridging oxygens (here, Mn−O−X) increase with increasing A/X and/or A/M radius ratios, indicating the trend to the ideal cubic ($Fd\bar{3}m$) structure typified by $CsAlO_2$. The sublattices of the magnetic Mn^{2+} ions in both structure types under study ($Pmn2_1$ and Pn) are essentially the same; namely, they are pseudocubic eutaxy with 12 nearest neighbors. The magnetic properties of the four new phases plus Li_2MnSiO_4 were characterized by carrying out magnetic susceptibility, specific heat, magnetization, and electron spin resonance measurements and also by performing energy-mapping analysis to evaluate their spin exchange constants. Ag_2MnSiO_4 remains paramagnetic down to 2 K, but A_2MnXO_4 (A = Li, Na; X = Si, Ge) undergo a three-dimensional antiferromagnetic ordering. All five phases exhibit short-range AFM ordering correlations, hence showing them to be low-dimensional magnets and a magnetic field induced spin-reorientation transition at $T < T_N$ for all AFM phases. We constructed the magnetic phase diagrams for A_2MnXO_4 (A = Li, Na; X = Si, Ge) on the basis of the thermodynamic data in magnetic fields up to 9 T. The magnetic properties of all five phases experimentally determined are well explained by their spin exchange constants evaluated by performing energy-mapping analysis.

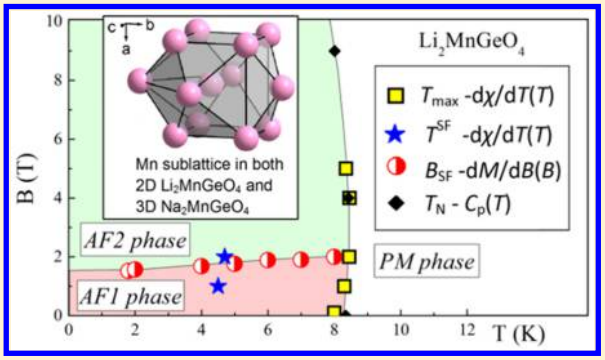

1. INTRODUCTION

Compounds of the A_2MXO_4 family (A = Li, Na, Ag; M = Be, Mg, Mn, Fe, Co, Zn, Cd; X = Si, Ge) present a variety of tetrahedral structure types and physical properties. Li_2MSiO_4 (M = Mn, Fe, Co) have been intensely studied as materials for positive electrodes of lithium-ion batteries.[1−11] Their sodium counterparts are of interest for sodium-ion batteries[12−14] or capacitors.[15] Ag_2ZnGeO_4 has attracted attention as a photocatalyst[16,17] and Li_2CoGeO_4 as an oxygen evolution catalyst.[18] Several phases of this family are solid-state Na^+ or Ag^+ cation conductors[19−24] and hosts for luminescent ions.[25−29] The most intensely studied members of this family are based on magnetic cations M^{2+} = Mn, Fe, and Co, but surprisingly little is known about their magnetic structures and properties. Only Na_2CoXO_4 (X = Si, Ge)[30,31] and Li_2MSiO_4 (M = Mn, Fe, Co)[3,6,7,11,30,32,33] have been studied in some detail. Five of the six possible Mn^{2+} compounds of this family, however, remain unexplored regarding magnetism.

The present work is concerned with the manganese compounds, namely, A_2MnSiO_4 (A = Li, Na, Ag) and A_2MnGeO_4 (A = Li, Na). The indexed powder diffraction patterns of these five compounds were reported by us earlier,[34] and the crystal structure of Li_2MnSiO_4 ($P2_1/n$) was also

Received: August 22, 2017
Published: October 31, 2017

DOI: 10.1021/acs.inorgchem.7b02130
Inorg. Chem. 2017, 56, 14023−14039

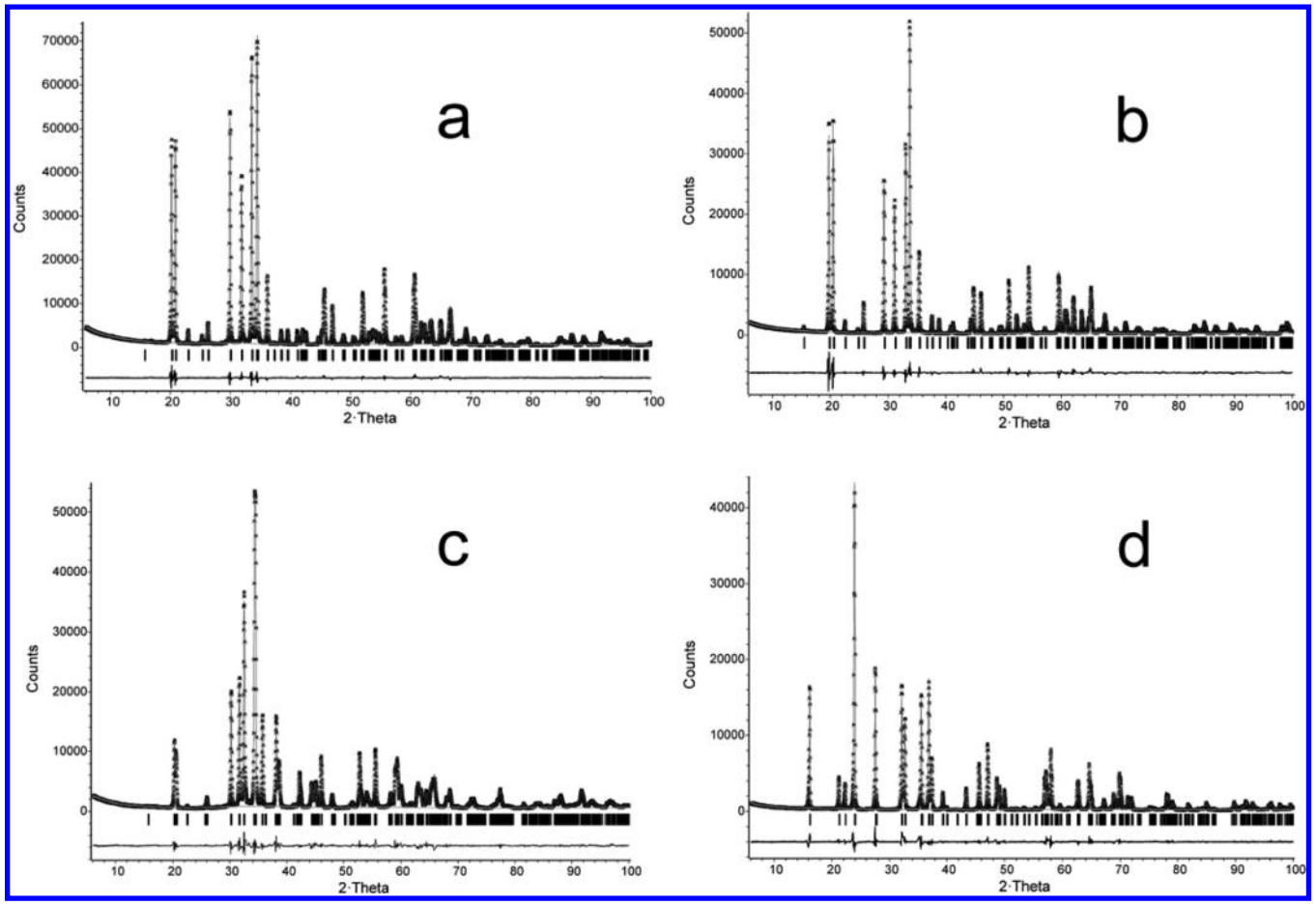

Figure 1. Experimental XRD patterns and Rietveld refinement results: (a) Na_2MnSiO_4, (b) Na_2MnGeO_4, (c) Ag_2MnSiO_4, and (d) Li_2MnGeO_4. Stars, experimental points; gray lines, calculated profiles; thick light gray line, background; vertical bars, Bragg positions; bottom lines, difference profiles.

reported.[4,33] There is only a brief mention of the lattice parameters for Li_2MnGeO_4 ($Pmn2_1$) without any structural detail,[35] and a density functional theory (DFT) study on Na_2MnSiO_4 (Pn) with diffraction data only used for lattice parameter refinement.[10] Here, we report the preparation, crystal structures, and magnetic properties of A_2MnSiO_4 (A = Na, Ag) and A_2MnGeO_4 (A = Li, Na) as well as a more careful study of the magnetism of Li_2MnSiO_4. We evaluate the spin exchange interactions of these five compounds by performing the energy-mapping analysis[36,37] based on DFT calculations and discuss their magnetic properties.

2. EXPERIMENTAL SECTION

Starting materials were reagent-grade alkali carbonates, manganese oxide, germanium oxide, zinc oxide, cadmium oxide, hydrous silica, and silver nitrate. The carbonates and GeO_2 were dried at 420 K, and CdO was calcined at 900 K. $SiO_2{\cdot}xH_2O$ and MnO_y were analyzed by weight change on calcinations at 1270 K (to give SiO_2) and 1020 K (to give phase-pure Mn_2O_3), respectively, and then used in their pristine forms. A_2MnXO_4 (A = Li, Na) were obtained from carefully mixed stoichiometric amounts of the reagents by conventional solid-state reactions in flowing hydrogen (X = Si) or nitrogen (X = Ge) with intermittent grindings and pressings. The temperatures of the final heat treatments were 1250 K for both germanates, 1220 K for Na_2MnSiO_4, and 1320 K for Li_2MnSiO_4. The diamagnetic analogues Li_2CdGeO_4[38] and Na_2ZnSiO_4[39,40] were prepared similarly in air at 1170 K. Ag_2MnSiO_4 was prepared from Na_2MnSiO_4 by ion exchange in slight excess of molten $AgNO_3$ for 2 h at 570 K, which was followed by washing with distilled water and drying. The silver content was determined by thiocyanate titration after digestion in hot H_2SO_4 and dilution. The phase purity of all prepared compounds was verified by powder X-ray diffraction (XRD). Scans for the structure analysis were performed with Cu Kα radiation using a rotating-anode D/max-RC diffractometer (Rigaku, Japan) equipped with a secondary beam graphite monochromator. For Rietveld refinements, the GSAS +EXPGUI suite was used.[41,42]

The magnetic properties were measured using a Quantum Design SQUID XL-5 magnetometer. The temperature dependence of magnetic susceptibility $\chi = M/B$ was measured in the temperature range 1.8−300 K at the magnetic field $B = 0.1$ T and in the T range 2−20 K in various applied fields $B \leq 5$T. The isothermal magnetization curves M vs B were recorded for magnetic fields $B \leq 5$T at various temperatures $T < T_N$ after cooling the sample in zero field. The specific heat measurements were carried out by a relaxation method using a Quantum Design PPMS system. The plate-shaped samples of Li_2MnGeO_4, Li_2CdGeO_4, Na_2MnSiO_4, Na_2ZnSiO_4, and Li_2MnSiO_4 of ∼0.2 mm thickness and 4−6 mg mass used for the experiments were obtained by cold pressing of the polycrystalline powder. The data were collected at zero magnetic field and under applied fields up to 9 T in the temperature range 1.9−280 K. Electron spin resonance (ESR) studies were carried out using an X-band ESR spectrometer CMS 8400 (ADANI) ($f \approx 9.4$ GHz, $B \leq 0.7$ T) equipped with a low-temperature mount operating in the range $T = 7$−300 K. The effective g-factors of our samples were calculated with respect to an external reference for the resonance field using BDPA (a,g-bisdiphenyline-b-phenylallyl) as the reference material, for which $g_{ref} = 2.00359$.

DOI: 10.1021/acs.inorgchem.7b02130
Inorg. Chem. 2017, 56, 14023−14039

Table 1. XRD Refinement Details for A_2MnXO_4

	Li_2MnGeO_4	Na_2MnSiO_4	Na_2MnGeO_4	Ag_2MnSiO_4
formula weight	205.4	193.0	237.5	362.7
crystal system	orthorhombic	monoclinic	monoclinic	monoclinic
space group	$Pmn2_1$	$P1n1$	$P1n1$	$P1n1$
temperature of data collection (K)	301	307	301	298
a (Å)	6.46751(7)	7.02857(7)	7.16427(8)	6.93888(8)
b (Å)	5.47639(5)	5.60957(5)	5.72970(7)	5.64791(7)
c (Å)	5.05380(5)	5.33391(5)	5.40710(6)	5.50969(7)
β (deg)	90	89.7949(13)	90.109(2)	90.3942(13)
V (Å^3)	179.00	210.30	221.96	215.92
Z	2	2	2	2
R_{wp}	0.0884	0.0726	0.0963	0.0667
R_{exp}	0.0326	0.0205	0.0276	0.0226
$R\|F\|^2$	0.02991	0.04033	0.05102	0.02826

Table 2. Important Interatomic Distances (Å) and Bond Angles (deg) in A_2MnXO_4[a]

	Li_2MnGeO_4	Na_2MnGeO_4	Na_2MnSiO_4	Ag_2MnSiO_4
X−O	1.744(5)	1.687(7)	1.541(4)	1.602(10)
	1.747(5)	1.737(4)	1.555(3)	1.667(13)
	1.765(4)×2	1.838(5)	1.616(3)	1.695(11)
		1.935(4)	1.715(3)	1.695(12)
average	1.76	1.80	1.61	1.66
sum of ionic radii[43]	1.77		1.64	
Mn−O	2.053(4)×2	1.840(10)	2.007(5)	1.962(9)
	2.106(6)	1.892(7)	2.079(5)	2.002(12)
	2.156(6)	2.092(7)	2.082(6)	2.016(10)
		2.120 (7)	2.086(4)	2.111(11)
average	2.09	1.99	2.06	2.02
sum of ionic radii[43]	2.04			
A1-O	1.869(16)	2.147(4)	2.255(5)	2.319(10)
	1.969(12)	2.259(8)	2.285(3)	2.359(10)
	2.011(9)	2.345(5)	2.476(3)	2.460(11)
	2.021(11)	2.558(5)	2.484(3)	2.469(11)
average	1.97	2.33	2.38	2.40
sum of ionic radii[43]	1.97	2.37		2.38
A2−O		2.235(4)	2.166(3)	2.230(12)
		2.358(10)	2.300(5)	2.342(10)
		2.397(5)	2.370(3)	2.354(12)
		2.424(5)	2.386(3)	2.383(11)
average		2.35	2.31	2.33
sum of ionic radii[43]		2.37		2.38
Mn−Mn	4.535 × 4	4.905 × 2	4.858 × 2	4.941 × 2
	5.054 × 2	4.912 × 2	4.872 × 2	4.967 × 2
	5.424 × 4	5.407 × 2	5.334 × 2	5.510 × 2
	5.476 × 2	5.730 × 2	5.610 × 2	5.591 × 2
		5.840 × 2	5.662 × 2	5.615 × 2
		5.846 × 2	5.674 × 2	5.648 × 2
angles: Mn−O1−X	115.6(2)×2	118.4(2)	124.3(2)	130.0(6)
Mn−O2−X	110.1(2)	120.6(2)	125.1(2)	132.2(5)
Mn−O3−X	108.8(2)	128.9(2)	132.5(2)	127.0(6)
Mn−O4−X		133.4(2)	126.9(2)	125.8(6)
average	112.5	125.3	127.2	128.8

[a]Minor Li/Mn mixing in Li_2MnGeO_4 and minor Na substitution for Ag in Ag_2MnSiO_4 are ignored in this table but are indicated in Table S2 of the Supporting Information.

3. RESULTS AND DISCUSSION

3.1. Crystal Structures. The experimental, calculated, and difference XRD profiles for the four compounds are shown in Figure 1. Details of the XRD refinements are summarized in Table 1; the important interatomic distances and bond angles are in Table 2, and details of data collection are presented in Table S1. The atomic coordinates and isotropic thermal parameters are listed in Table S2. Table S3 compares lattice parameters of the new phases with those for the previously known analogues.

DOI: 10.1021/acs.inorgchem.7b02130
Inorg. Chem. 2017, 56, 14023−14039

Li_2MnGeO_4 is light gray, a typical color of high-spin Mn^{2+} (d^5) compounds. Its XRD pattern was completely indexed in the orthorhombic system. The sole independent systematic absence is found for the reflections $h0l$ ($h + l$ odd absent). This indicates two possible space groups: $Pmnm$ and $Pmn2_1$. The overall similarity of the XRD pattern with that for Li_2CdGeO_4[38] suggests the latter group as the most probable. With the crystal structure of Li_2CdGeO_4 taken as a starting model, the refinement converged rapidly to reasonable reliability factors. The unit cell volumes correlate with ionic sizes (Table S3 of the Supporting Information); the average bond lengths of Li−O and Ge−O agree well with the corresponding ionic radii sums, but two of the four Mn−O distances are somewhat longer than expected (Table 2). In contrast to the Cd prototype, a small degree of Li/Mn mixing was found in this structure. This is so because the ionic radii of Mn^{2+} and Li^+ are similar.

Both Na_2MnSiO_4 and Na_2MnGeO_4 are light brown. This darkening may be attributed to their partial oxidation in air, which leads to the extraction of sodium, hence forming a mixed-valence state $Mn^{2+/3+}$ on the surface. Indeed, XPS study of Na_2MnSiO_4 shows very weak peaks from silicon and manganese but strong peaks from sodium, carbon, and oxygen, indicating that the surface layer consists mostly of Na_2CO_3. The weak response from Mn is in reasonable agreement with that from MnO, although admixture of Mn^{3+} cannot be excluded. In any case, this is only a surface layer, whereas all bulk properties (ESR, magnetization, bond lengths, etc.) unambiguously correspond to Mn^{2+}, as shown below. The associated deviation from the stoichiometry is too small to be detected from the refined Na site occupancies. In general, color changes and ESR are much more sensitive to the presence of mixed valence than most analytical methods.

The powder patterns for both sodium compounds might be indexed in an orthorhombic system with unit cell parameters similar to those for Li_2MnGeO_4 (only slightly larger, in accordance with the larger size of Na^+, see Table 1), and even systematic absences were the same. However, the accuracy of the fit was much worse compared with the case of Li_2MnGeO_4, especially for the silicate. This indicated that the true symmetry is lower. Moreover, the relative intensities differed drastically, indicating another structure type. We note a strong analogy with the family of monoclinic phases having space group $P1n1$ with angle β very close to 90°, typified by Na_2ZnXO_4 (X = Si, Ge).[39,40] This nonstandard setting for the space group 7 is preferred to the standard one, $P1c1$, to make the pseudo-orthorhombic metrics evident and facilitate the comparison with truly orthorhombic counterparts. The same holds for Li_2MnSiO_4 ($P12_1/n1$ instead of $P12_1/c1$). Thus, the space group for Na_2MnGeO_4 in the PDF card 00-56-94 should be changed from $Pmn2_1$ to $P1n1$. The XRD pattern of Ag_2MnSiO_4 (PDF card 00-55-699) was initially indexed with doubled c-axis, but this resulted only from a typo in one 2Θ value. After correcting the typo, the pattern was completely indexed with a small unit cell analogous to that of the sodium precursor.

Taking the Zn analogues for the starting models, the crystal structures of Na_2MnXO_4 (X = Si, Ge) and Ag_2MnSiO_4 were successfully refined. The unit cell volumes show reasonable correlations with the ionic radii (Table S3 of the Supporting Information). Differences between the average bond lengths and the corresponding sums of ionic radii do not exceed 0.06 Å in all cases (Table 2). In contrast to Li_2MnGeO_4, no A/Mn mixing was found, which is due to the larger differences in ionic radii. In Ag_2MnSiO_4, however, our analytical data indicated somewhat reduced Ag content (found, 57.7 wt %; calcd 59.5 wt %) due to an incomplete ion exchange. Therefore, mixed Ag/Na occupancy was refined in the two independent silver sites and resulted in Na fractions of ∼0.02 and ∼0.07 (Table S2 of the Supporting Information). Thus, the true formula should be $Ag_{1.91}Na_{0.09}MnSiO_4$ with 58.0 wt % Ag, in reasonable agreement with the titration data. This minor Na impurity will be ignored for simplicity in our further discussion.

3.2. Crystal−Chemistry Relations between the Tetrahedral Structures. The structural results of our work on A_2MnGeO_4 (A = Li, Na) and A_2MnSiO_4 (A = Na, Ag) were compared in Figure 2 with the previously reported structure of

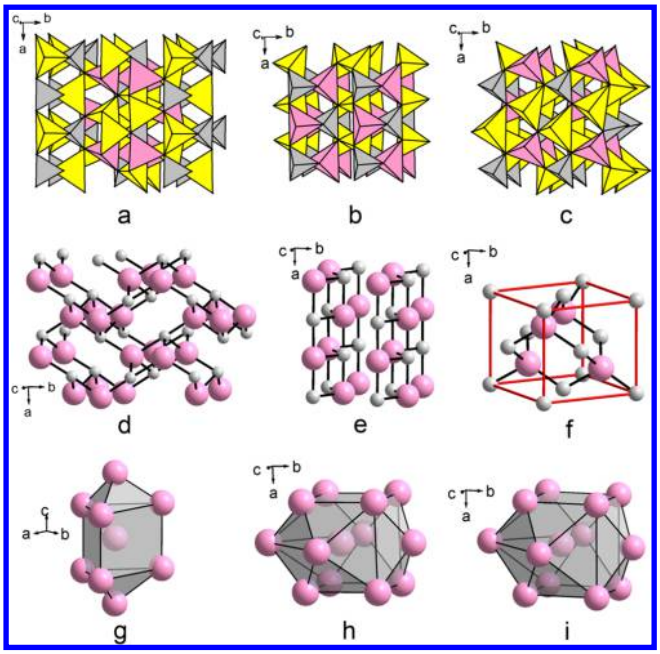

Figure 2. Crystal structures of (a, d, and g) Li_2MnSiO_4, (b, e, and h) Li_2MnGeO_4, and (c, f, and i) Na_2MnGeO_4. (a, b, and c) Polyhedral views with the AO_4, MnO_4, and XO_4 tetrahedra in yellow, pink, and gray, respectively. (d, e, and f) Topology of the rigid part of the structures $(MnXO_4)^{2-}$, where Mn and X atoms are pink and gray balls, respectively. The O and A atoms are omitted, the bent Mn−O−X bridges are shown as black straight lines, and the sphalerite-type pseudocell is outlined in red. (g, h, and i) Packing modes of the magnetic cations Mn are shown as a coordination polyhedron.

Li_2MnSiO_4 ($P2_1/n$).[4] The three new Pn structures are very similar, and Na_2MnGeO_4 (Figures 2c, f, and i) effectively represents all of them. Although the three structure types of Figure 2 are essentially different, they have several features in common:

(1) All of them are based on a double-layered hexagonal close packing of oxygen anions; however, there are no close contacts between anions, so the term "eutaxy"[44] is more appropriate.
(2) All cations and anions have distorted tetrahedral environments (Figures 2a−c).
(3) Both $Pmn2_1$ and Pn structures may be described as superlattices of the ZnO (or wurtzite) type. All cation-centered tetrahedra are in the same orientation, sharing only the vertices. The phases are noncentrosymmetric and hence are piezoelectric. In the $P2_1/n$ structure of Li_2MnSiO_4, one-half of the tetrahedra have the opposite orientation to that the other half tetrahedra do, so that

DOI: 10.1021/acs.inorgchem.7b02130
Inorg. Chem. 2017, 56, 14023−14039

the parameter b is doubled, the structure is centrosymmetric, and couples of LiO_4 tetrahedra share edges.

(4) Both monoclinic structures ($P2_1/n$ and Pn) have a three-dimensional (3D) framework, whereas the $Pmn2_1$ structure is layered (Figures 2d–f).

(5) The Pn structure type has the topology of a cristobalite where arrangement of Mn and X is of slightly distorted sphalerite type (Figure 2f), so it is natural that the Mn sublattice is a pseudocubic eutaxy in which each Mn has 12 Mn neighbors in the form of a distorted cuboctahedron (Figure 2i). Unexpectedly, essentially the same Mn arrangement is found in the layered $Pmn2_1$ structure (Figure 2h). In the $P2_1/n$ structure (Figure 2g), the six nearest Mn neighbors form a distorted trigonal prism with distances to the central Mn of 4.14–4.74 Å and two more neighbors at 5.07 Å capping the prism.

In the four new structures Li_2MnGeO_4, Na_2MnGeO_4, Na_2MnSiO_4, and Ag_2MnSiO_4, the longest and shortest Mn···Mn distances within the distorted cuboctahedra (Figures 2h and i) differ by only 20.8, 19.2, 16.8, and 14.3%, respectively (Table 2), demonstrating a gradual approach to the cubic metrics (see below).

The substitution of smaller Mn^{2+} for Cd^{2+} in the layered structure of Li_2CdGeO_4 reduces the lattice parameters a and c while either unchanging or slightly increasing the b parameter (Table S3 of the Supporting Information). This is quite natural because the $(MGeO_4)^{2-}$ layers are parallel to the ac plane, and only the parameters parallel to this layer strongly depend on the size of M^{2+}. As the coordination polyhedron of the interlayer ion (here, LiO_4) contracts in the ac plane, it expands in the perpendicular direction to maintain normal bond lengths; this may compensate for contraction of the rigid layer in the same direction. This behavior is typical of layered structures.[45]

Each oxygen anion in the structures A_2MnXO_4 has a distorted tetrahedral environment of two A, one Mn, and one X atom. In the three compounds with large monovalent cations Na^+ and Ag^+, all angles between the strongest bonds, O–X and O–Mn (Table 2), are considerably larger than the ideal tetrahedral value of 109.5°. In Li_2MnGeO_4, this deviation is small, and the same was observed in Li_2MnSiO_4 ($P2_1/n$),[4] where the average Si–O–Mn angle is equal to 117.0°. Assuming the lone pair repulsion and/or hard sphere repulsion to be the main factors affecting the bond angles, one would expect exactly the opposite trend. Therefore, alternative explanations are needed. One of them may be purely ionic: the largest angle would be the one between the multiply charged cations. However, a more plausible explanation is based on the structural topology.

In the ZnO-derived structures, the ideal tetrahedral angles require all four cations to be equal in size. With large size differences between mono- and polyvalent cations, the structures are better understood as cristobalite-type $(MXO_4)^{2-}$ frameworks stuffed with A^+. Increasing the size of the A^+ cations requires more space for them. The only way to expand the framework with constant X–O and M–O bond lengths is to increase X–O–M angles, approaching the ideal value of 180° found in cubic $CsAlO_2$.[46] This trend was probably first noted in the orthorhombic ($Pbca$) $AFeO_2$ series (A = K, Rb, Cs)[47] and is further supported by Figure 3 combining the data for all known A_2RXO_4 isomorphs of the Pn type and some structurally related orthorhombic ($Pna2_1$) gallates and aluminates.

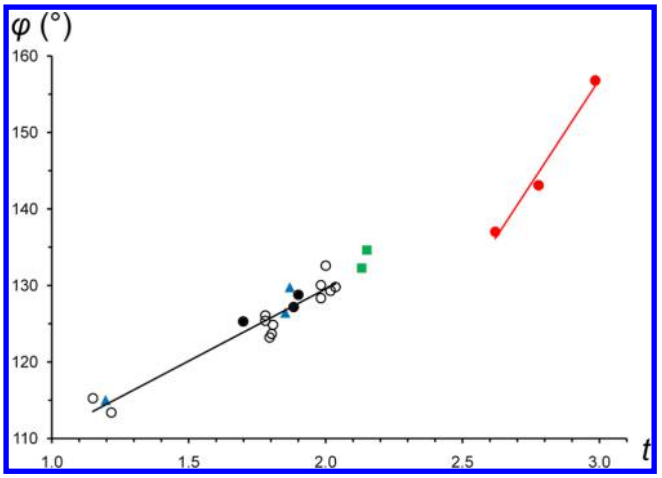

Figure 3. Correlation between average bond angle φ, MOX or MOM, and Shannon's[43] radius ratio t of extra-framework and framework cations in the three families of stuffed cristobalites, Pn A_2MXO_4 (black circles), $Pna2_1$ AMO_2 (blue triangles, M = Ga; green squares, M = Al), and $Pbca$ $AFeO_2$ (red circles). $t = {}^{IV}R(A^+) \times 2/[{}^{IV}R(M^{2+}) + {}^{IV}R(X^{4+})]$ for A_2MXO_4, $t = {}^{IV}R(A^+)/{}^{IV}R(M^{3+})$, and $t = {}^{VIII}R(A^+)/{}^{IV}R(Fe^{3+})$ for $AFeO_2$. Phases, left to right: Li_2ZnGeO_4,[48] $LiGaO_2$,[49] Li_2MnSiO_4 (by DFT only),[10] **Na_2MnGeO_4**, Na_2ZnGeO_4 (two points),[29,39] Ag_2ZnGeO_4,[24] Li_2BeSiO_4,[50] Na_2CoGeO_4,[51] $NaGaO_2$,[52] $AgGaO_2$,[53] **Na_2MnSiO_4**, **Ag_2MnSiO_4**, Na_2ZnSiO_4 (two points),[39,40] Ag_2ZnSiO_4,[24] Na_2CoSiO_4,[14b] Na_2MgSiO_4,[19] $NaAlO_2$,[54] $AgAlO_2$,[55] $KFeO_2$,[47] $RbFeO_2$,[47] $CsFeO_2$.[47] Filled black circles and formulas in bold correspond to the three new phases from the present work. The data for Li_2CoGeO_4 (Pn)[18] were not included because of impossible interatomic distances.

Interestingly enough, the trend toward the ideal cubic structure, evident from the evolution of X–O–Mn bond angles and Mn···Mn distance ratios discussed above, could not be deduced from the evolution of the lattice parameters. The ratios of the three pseudocubic cell edges do not show regular approaching unity on silver substitution for sodium in Na_2RSiO_4 (R = Zn, Mn) and Na_2ZnGeO_4 (see Table S3 of the Supporting Information) as well as in the $AFeO_2$ series (A = K, Rb, Cs).[47] On heating, too, the pseudocubic cell edges of $KFeO_2$ and $RbFeO_2$ initially diverge and converge only in the vicinity of the othorhombic-to-cubic phase transition.[47]

3.3. Magnetic Susceptibility. The temperature-dependent magnetic susceptibilities $\chi = M/B$ determined for Li_2MnSiO_4, Na_2MnSiO_4, Ag_2MnSiO_4, Li_2MnGeO_4, and Na_2MnGeO_4 are presented in Figure 4. Except for Ag_2MnSiO_4, the χ vs T plots exhibit a sharp peak at a low temperature, suggesting the occurrence of a long-range antiferromagnetic (AFM) ordering. A closer look at the data displays a broad susceptibility maximum χ_{max} at T_{max} and a sharp peak at slightly lower temperature. The magnetic specific heat, $\partial(\chi T)/\partial T$, shows a pronounced λ-shape anomaly (for example, see Figure 5 for Li_2MnSiO_4). This allows one to determine the Néel temperature T_N, below which a long-range AFM ordering takes place. Our analysis shows that $T_N = 10.3 \pm 0.5$ for Li_2MnSiO_4, 4.1 ± 0.5 K for Na_2MnSiO_4, 8.1 ± 0.5 K for Li_2MnGeO_4, and 4.0 ± 0.5 K for Na_2MnGeO_4. The T_{max} appears at 0.5 to 2 K above T_N. Such a behavior is found for low-dimensional magnetic systems for which the χ_{max} arises from a short-range AFM

DOI: 10.1021/acs.inorgchem.7b02130
Inorg. Chem. 2017, 56, 14023–14039

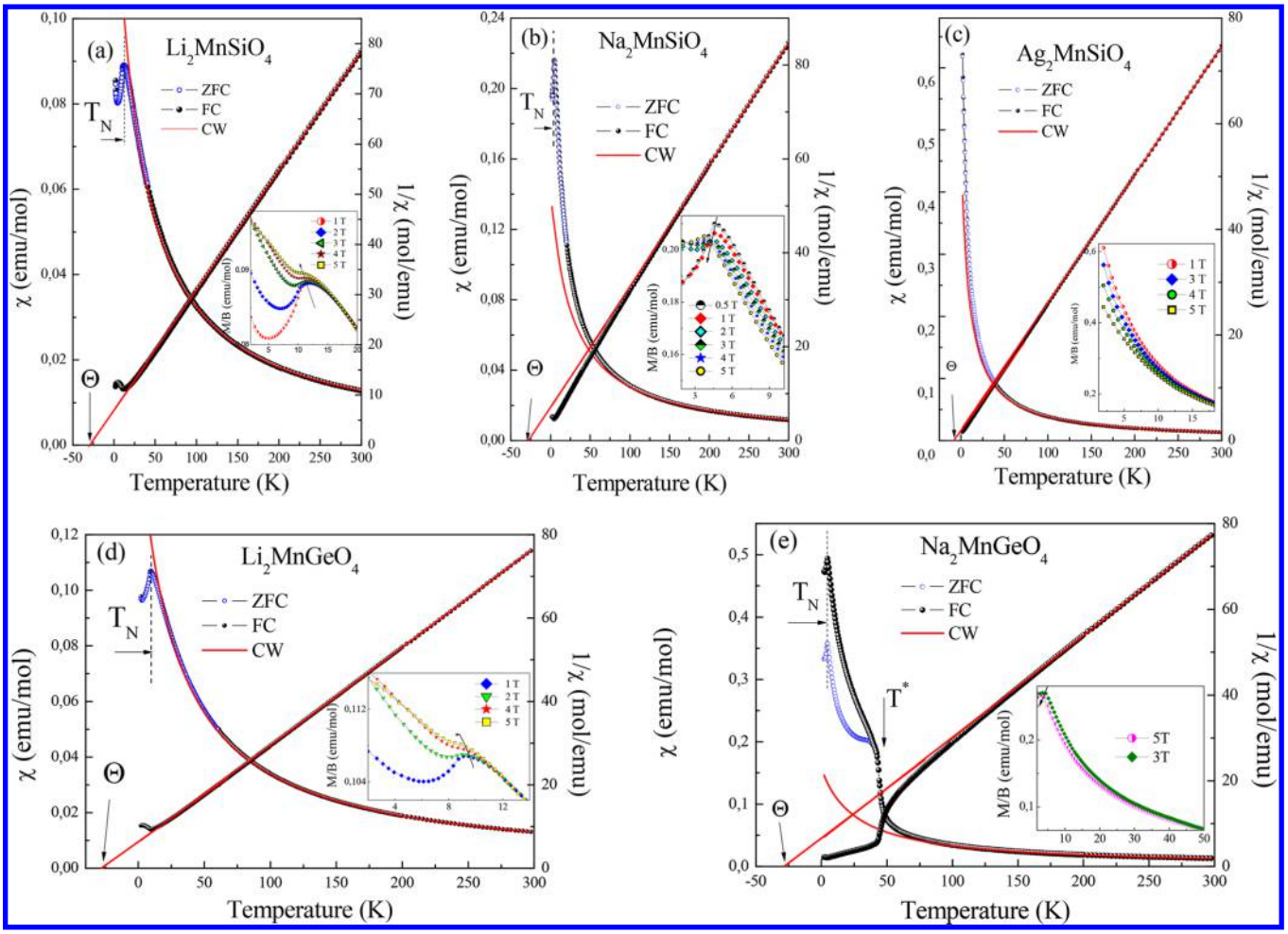

Figure 4. Temperature dependence of the magnetic susceptibility and its inverse measured at B = 0.1 T for (a) Li_2MnSiO_4, (b) Na_2MnSiO_4, (c) Ag_2MnSiO_4, (d) Li_2MnGeO_4, and (e) Na_2MnGeO_4. The red solid curves represent an approximation in accordance with the Curie–Weiss law.

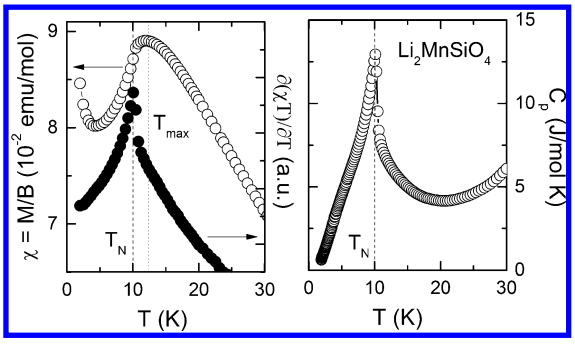

Figure 5. (a) Magnetic susceptibility obtained at B = 0.1 T, associated magnetic specific heat, and (b) specific heat of Li_2MnSiO_4 at $T \leq 30$ K. The dashed line shows the position of the λ-like anomaly at T_N; the dotted line indicates a broad correlation maximum in χ at T_{max} (see the text).

ordering that takes place above T_N, and the long-range order occurs at temperatures lower than those suggested by mean field theory.[56] In contrast, the magnetic susceptibility of Ag_2MnSiO_4 shows a Curie–Weiss behavior over the whole temperature range down to 1.8 K, implying the absence of a long-range magnetic order (Figure 4c).

The temperature-dependent magnetic susceptibility of Na_2MnGeO_4 shows a rather complicated behavior with additional anomaly at $T^* \approx 43$ K (Figure 4e), which is associated with an increase in the magnetization by $\sim 3 \times 10^{-3}$ μ_B per formula unit (f.u.). There occurs a clear discrepancy between the ZFC and FC curves at $T < T^*$. Correspondingly, the inverse susceptibility deviates strongly from the Curie–Weiss behavior on approaching the T^* anomaly. In applied magnetic fields, the T_N shifts slightly to lower temperatures for all samples, and the T^* anomaly disappears (see the inset of Figure 4e). Therefore, this anomaly can be related to the presence of a ferromagnetic impurity, most probably a small amount of Mn_3O_4. Indeed, a careful inspection of the XRD pattern revealed the presence of very weak reflections from Mn_3O_4 (and also from MnO) not detected in our initial XRD study and not accounted for in the Rietveld analysis. Exactly the same situation was described in a recent investigation of $Mn_2Sb_2O_7$: a minor impurity of Mn_3O_4 was overlooked by XRD but detected by magnetic measurements.[57]

For all five phases Li_2MnSiO_4, Na_2MnSiO_4, Ag_2MnSiO_4, Li_2MnGeO_4, and Na_2MnGeO_4, the magnetic susceptibilities at $T > 70$ K are nicely described by the Curie–Weiss law:

$$\chi = \chi_0 + \frac{C}{T - \Theta} \quad (1)$$

where χ_0 is the temperature-independent susceptibility, Θ the Weiss temperature, and C the Curie constant $C = N_A \mu_{eff}^2 \mu_B^2 / 3k_B$ (N_A = Avogadro's number, μ_{eff} = the effective magnetic moment, μ_B = Bohr magneton, and k_B = Boltzmann constant).

DOI: 10.1021/acs.inorgchem.7b02130
Inorg. Chem. 2017, 56, 14023–14039

Table 3. Values of T_N (in K), Θ (in K), and μ_{eff} (in μ_B) of A_2MnXO_4 from Magnetic Susceptibility Measurements and g-Factor of A_2MnXO_4 from ESR Measurements

	T_N	Θ	$f = \lvert\Theta\rvert/T_N$	μ_{eff}	g
Li_2MnSiO_4	10.1	−30 ± 1	3.0	5.78	1.99
	12[33]	−38	3.2	5.7	
	12[6]	−29	2.4	6	2.003
					2.00[11]
	12[32]	−35	2.9	6	
	12[7]	−29.4	2.5	5.85	
Na_2MnSiO_4	4.2 ± 0.5	−27 ± 1	6.4	5.58	1.99
Ag_2MnSiO_4		−9 ± 1	>5	5.78	2.01
Li_2MnGeO_4	8.1	−27 ± 1	3.5	5.89	1.99
Na_2MnGeO_4	4.0	−27 ± 1	6.8	5.81	1.99

We estimated χ_0 by summing Pascal's constants.[58] The parameters for the five phases extracted from fitting the experimental data in the range 200−300 K are summarized in Table 3, and those of the related silicates and germanates available in the literature are in Table S4 of the Supporting Information. The effective magnetic moments μ_{eff} calculated from the corresponding Curie constants were found to be in reasonable agreement with theoretical estimates $\mu_{theor}^2 = g^2\mu_B^2 S(S+1)$ using the effective g-factors (Table 3) determined from the ESR data (see below). Our analysis yields negative Θ values for all five compounds, indicating the presence of predominant AFM interactions. For classical 3D AFM systems, frustration index $f=|\Theta|/T_N$ usually takes values of 1−3. Considerably larger values would signal a presence of the marked spin frustration. Obviously, such frustration can hamper the onset of the long-range ordering.[59] The f values of Li_2MnSiO_4 and Li_2MnGeO_4 are smaller than 4, so it is not surprising that they undergo a 3D AFM ordering. Na_2MnSiO_4 and Na_2MnGeO_4, however, have much larger f values (6.4 and 6.8, respectively), yet they also undergo a 3D AFM ordering. The T_N values of Na_2MnSiO_4 and Na_2MnGeO_4 are ∼4 K, which are approximately half the corresponding values of their Li-analogues (10.1 and 8.1 K, respectively) (Table 3).

The possible presence of ferromagnetic (FM) correlations in Na_2MnSiO_4 and Na_2MnGeO_4 can be inferred from the way their experimental $\chi(T)$ curves deviate from the Curie−Weiss law at low temperatures (Figures 4b, c, and e). A ferromagnetic (FM) contribution to the magnetization was pointed out earlier for other related compounds, particularly for Li_2FeSiO_4[3,32] and Li_2CoSiO_4,[33] and has been related to the presence of FM impurity phases by XRD data. For Li_2MnSiO_4, Na_2MnSiO_4, Ag_2MnSiO_4, and Li_2MnGeO_4, however, our magnetic studies (e.g., a visible hysteresis between ZFC and FC $\chi(T)$ curves) do not show any direct indication of such impurity. The available theoretical calculations also support such a scenario because they yield a very low energy difference (∼1 meV)[60] between FM and AFM quantum ground states for the Li−M^{2+} silicates and predict very similar effective magnetic moment values per high-spin transition-metal ions regardless of either the FM or AFM approach.[60−64] Moreover, as it was experimentally shown by Avdeev et al. from the neutron scattering studies, a quite complicated spin configuration is realized in magnetic sublattice for both Li_2MnSiO_4 and Li_2CoSiO_4, which contain AFM zigzag chains running along [001] and [101], respectively, forming corrugated FM layers of hexagons stacked perpendicular to these directions.[33]

The T_N, Θ, and μ_{eff} values obtained for Li_2MnSiO_4 in the present work are in reasonable agreement with those reported in the literature regardless of its polymorph structure (Table 3). This corroborates the conclusion of Bini et al. that the T_N value is influenced by the coexistence between transition ions in different oxidation states and the presence of the impurities rather than the polymorphism of Li−M^{2+} silicates.[32] Some difference in the Θ values (−29.4 to −38 K) is presumably caused by the uncertainty in the estimation of χ_0 and the different temperature regimes used for the Curie−Weiss fitting. The largest discrepancy in the reported Θ values was found for Li_2FeSiO_4, namely, Θ = −35 to −93.5 K[3,7,32] (Table S4 of the Supporting Information).

3.4. Specific Heat. The specific heat was measured for Li_2MnGeO_4, Na_2MnSiO_4, and Li_2MnSiO_4, which undergo a 3D AFM ordering as well as for nonmagnetic structural analogues of the first couple of phases: Li_2CdGeO_4 and Na_2ZnSiO_4. The specific heat data $C(T)$ for all Mn compounds at zero magnetic field exhibit a distinct λ-anomaly, which is a characteristic feature for a 3D AFM ordering (Figure 6). The values of T_N, deduced from $C(T)$ data at B = 0 T, are listed in Table 4. In applied magnetic fields, the λ-anomaly is slightly rounded and shifts to the lower temperature (see the lower right insets in Figure 6). To analyze the magnetic phase transition and evaluate the corresponding contribution to the specific heat and entropy in Li_2MnGeO_4 and Na_2MnSiO_4, we evaluated the lattice contribution to the specific heat by using the isostructural diamagnetic analogues (i.e., Li_2CdGeO_4 and Na_2ZnSiO_4, respectively). The Dulong−Petit value is $3R\nu$ = 199.54 J/(mol K), where R is the gas constant R = 8.314 J/(mol K) and ν is the number of atoms per formula unit (in the present case, ν = 8). As reported in Table 4, the magnitude of the λ-anomaly observed at T_N is noticeably smaller (1.5−1.8 times) than the one expected from the mean-field theory for the 3D antiferromagnetic ordering of a magnetic system with high-spin Mn^{2+} ion ($S = {}^5/_2$),[65] i.e., $\Delta C_p = 5R\nu S(S+1)/[(S+1)^2 + S^2]$ = 19.66 J/(mol K). Such a reduction of ΔC_p suggests that Li_2MnGeO_4, Na_2MnSiO_4, and Li_2MnSiO_4 are low-dimensional magnets and that a short-range AFM ordering is present above T_N.

Assuming that the $C(T)$ of a diamagnetic material provides a proper estimation for the pure lattice contribution to the specific heat, the magnetic contribution $C_m(T)$ can be estimated by using the scaling procedure.[66] In Figure 6a (6c) we compare the temperature dependence of the total specific heat for magnetic Li_2MnGeO_4 (Na_2MnSiO_4) and that of diamagnetic Li_2CdGeO_4 (Na_2ZnSiO_4) in the 160−280 K range. From these, we calculate the lattice part $C_{ph}(T)$ for the magnetic phase in the range 2−70 K. The Debye temperatures Θ_D, estimated using the $C(T) \propto T^3$ law in low temperature

DOI: 10.1021/acs.inorgchem.7b02130
Inorg. Chem. 2017, 56, 14023−14039

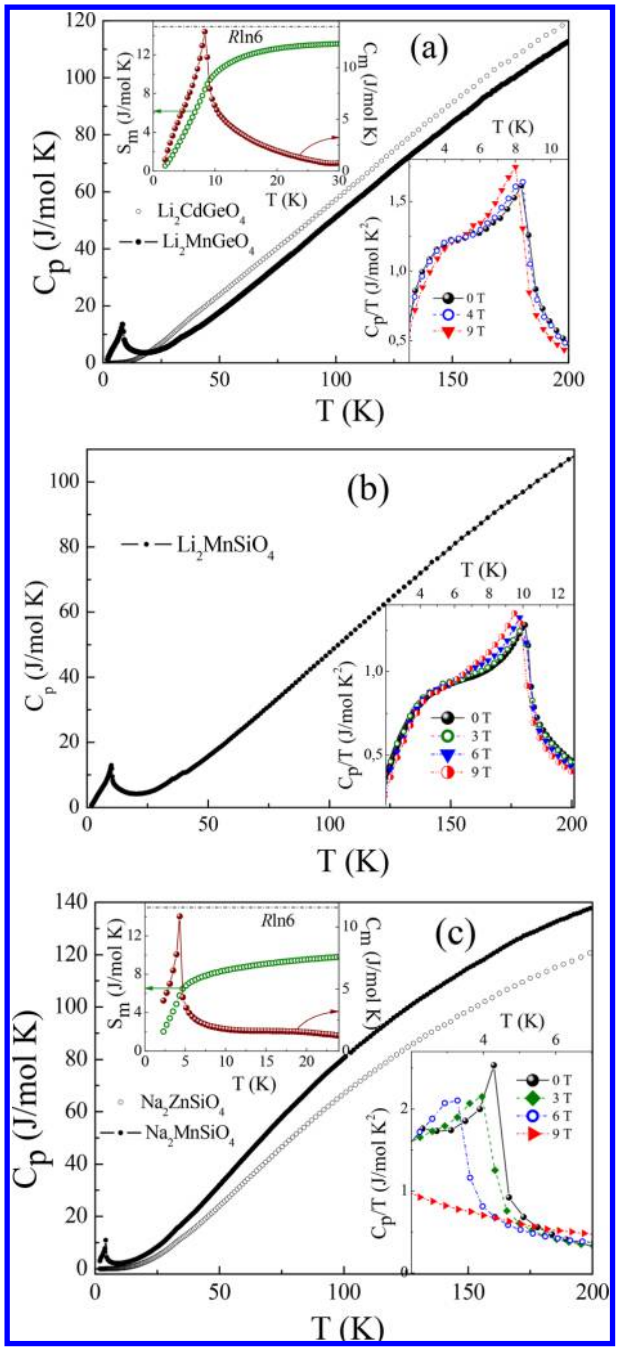

Figure 6. Temperature dependence of the specific heat C_p of (a) Li_2MnGeO_4 and its structural analogue Li_2CdGeO_4, (b) Li_2MnSiO_4, and (c) Na_2MnSiO_4 and its structural analogue Na_2ZnSiO_4 in zero magnetic field. Insets: (lower right) temperature dependence of C_p/T under different magnetic fields and (upper left) temperature dependence of $C_m(T)$ and the entropy $S_m(T)$.

range (2−18 K), are summarized in Table 4. The Debye temperatures for the magnetic systems were estimated by using the normalization procedure[65] in which the difference between the molar masses for Zn−Mn or Cd−Mn atoms is taken into account.

The magnetic entropy change was calculated using the equation:

$$\Delta S_m(T) = \int_0^T \frac{C_m(T)}{T} dT \quad (2)$$

Table 4. Thermodynamic Parameters of A_2MnXO_4 from Specific Heat Measurements

compound	T_N (K)	θ_D (K)	ΔS (J/mol K)	ΔC (J/mol K)	molar mass (g/mol)
Li_2MnGeO_4	8.1 ± 0.5	403.5	13.3	13.44	205.46
Li_2CdGeO_4		352.5			262.93
Na_2MnSiO_4	4.2 ± 0.5	394	10.6	10.88	193.00
Na_2ZnSiO_4		388			203.45
Li_2MnSiO_4	10.1 ± 0.5			12.5	160.90

which converges to a value smaller in magnitude than the one expected from the mean-field theory, $\Delta S_m = 2R\ln(2S + 1) \approx 14.9$ J/(mol K) (the dashed line in the upper left insets in Figure 6). The magnetic entropy released below T_N removes only about 30−40% of the saturation value, which is characteristic feature for a magnetic system with lower magnetic dimensionality.[67]

3.5. Field Dependence of the Magnetization. The magnetization curves $M(B)$ vs B for Li_2MnGeO_4, Li_2MnSiO_4, Na_2MnSiO_4, and Na_2MnGeO_4 determined at various temperatures in magnetic fields up to 5 T are presented in Figure 7. In this range of applied fields, the maximum of the magnetic moment remains essentially lower than the theoretically expected saturation magnetic moment for the high-spin Mn^{2+} ions ($S = {}^5/_2$): $M_s = gS\mu_B \approx 5\ \mu_B$/f.u. The magnetization curves exhibit a clear upward curvature, suggesting the presence of a field-induced spin-reorientation (spin-flop type) transition. The critical fields, B_{SF}, were determined from the maximum of the first derivative, $dM(B)/dB$, as indicated by arrows in Figure 7, and were used in constructing the magnetic phase diagrams (see Section 3.7). At $T = 2$ K, $B_{SF} \approx 1.6$ T for Li_2MnGeO_4, 2.2 T for Li_2MnSiO_4, and 1.8 T for Na_2MnSiO_4. Once again, the dependence $M(B)$ for Na_2MnGeO_4 demonstrates a more complicated character and reveals the presence of at least two different features at $B_{SF} \approx 1.6$ T and $B_{C1} \approx 0.8$ T at 2 K (Figure 7d). While B_{SF} vanishes above T_N, the second anomaly B_{C1} survives up to $T^* \approx 42$ K. Hence, it is reasonable to relate it to the FM impurity Mn_3O_4. With increasing temperature, the B_{SF} anomaly slightly shifts to higher fields, weakens in amplitude, and eventually disappears above T_N for all compounds.

The magnetization, M vs B, for the Ag_2MnSiO_4 sample (Figure 8) shows a rather different behavior. There is a slight bending in the B vs T curve, which is weaker than expected for a $S = {}^5/_2$ paramagnet. The magnetization tends to saturate at small magnetic fields reaching the maximum value of 4.5 μ_B/Mn^{2+} at 5 T, which is close to the theoretically expected full saturation value of the magnetization. The magnetization is well-described by a Brillouin function if a significant AFM mean field is considered (see Figure 8), which is phenomenologically given by

$$M = N_A g\mu_B BSB_S\left(\frac{g\mu_B BS}{k_B(T - \Theta^*)}\right) + \chi_0 T \quad (3)$$

where the parameter Θ^* is related to short-range AFM correlations between Mn spins in Ag_2MnSiO_4. The least-squares fitting according to eq 3 yields the best agreement with experimental data by using $g = 2.01$, $S = {}^5/_2$, and $\Theta^* \approx -5$ K (with $\chi_0 = -12 \times 10^{-5}$ emu/mol used for eq 1). The data hence confirm the absence of a long-range AFM order but imply the presence of AFM correlations at $T = 2$ K. $\Theta^* \approx -5$ K

DOI: 10.1021/acs.inorgchem.7b02130
Inorg. Chem. 2017, 56, 14023−14039

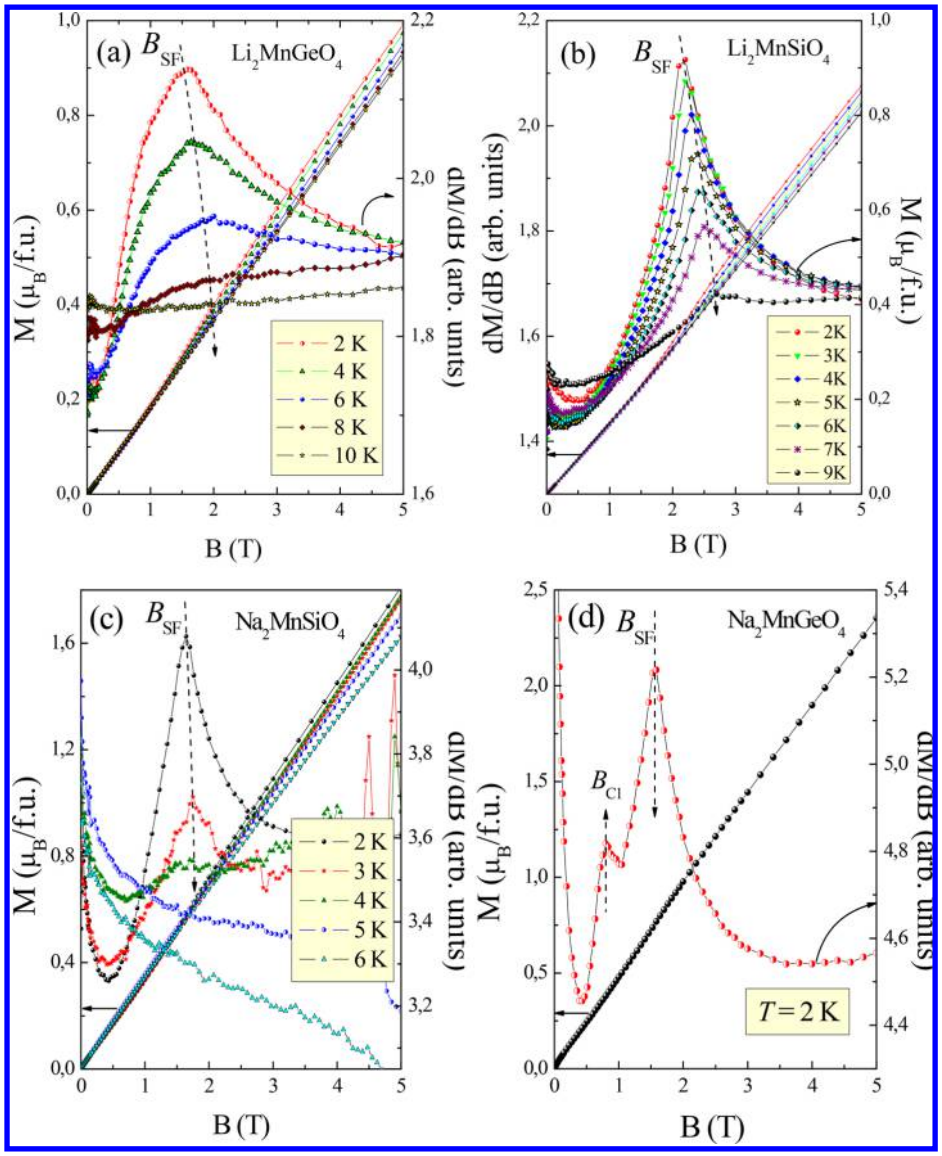

Figure 7. *M* vs *B* and d*M* vs d*B* plots determined for (a) Li_2MnGeO_4, (b) Li_2MnSiO_4, (c) Na_2MnSiO_4, and (d) Na_2MnGeO_4 at several different temperatures. The arrows point the positions of the field-induced phase transitions.

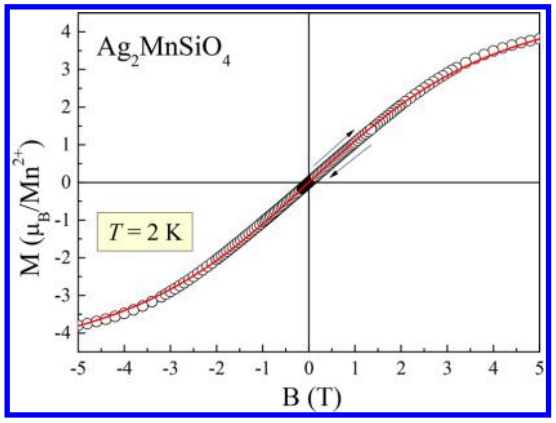

Figure 8. *M* vs *B* plot measured for Ag_2MnSiO_4 at *T* = 2 K. The circles are experimental data, and the red solid curve is the result of eq 3 (see text).

is consistent with the Curie–Weiss temperature Θ = −9 K (Table 3).

3.6. Electron Spin Resonance. All A_2MnXO_4 (A = Li, Na, Ag; X = Si, Ge) samples under study show a similar ESR response in the paramagnetic phase ($T > T_N$) and reveal a single exchange-narrowed absorption line ascribable to Mn^{2+} ions in tetrahedral coordination (Figure 9). A thorough analysis shows that for the better description of the line shape in the case of the A_2MnSiO_4 silicates, it is necessary to use two Lorentzians with significantly different relative intensities (for representative examples, see the insets of Figures 9a–c). The mode L_1 shown in blue in the insets of Figure 9a–c represents the main contribution to the absorption, and the second small absorption mode can be ascribed to the presence of a small amount of impurities in the samples. The main ESR parameters (namely, the effective *g*-factor, the ESR line width, and the integral ESR intensity) were deduced by fitting the experimental spectra with either one (for A_2MnGeO_4) or two (for A_2MnSiO_4) Lorentzian profiles to take into consideration the two circular components of the exciting linearly polarized microwave field on both sides of *B* = 0 because the ESR line is relatively broad,

DOI: 10.1021/acs.inorgchem.7b02130
Inorg. Chem. 2017, 56, 14023–14039

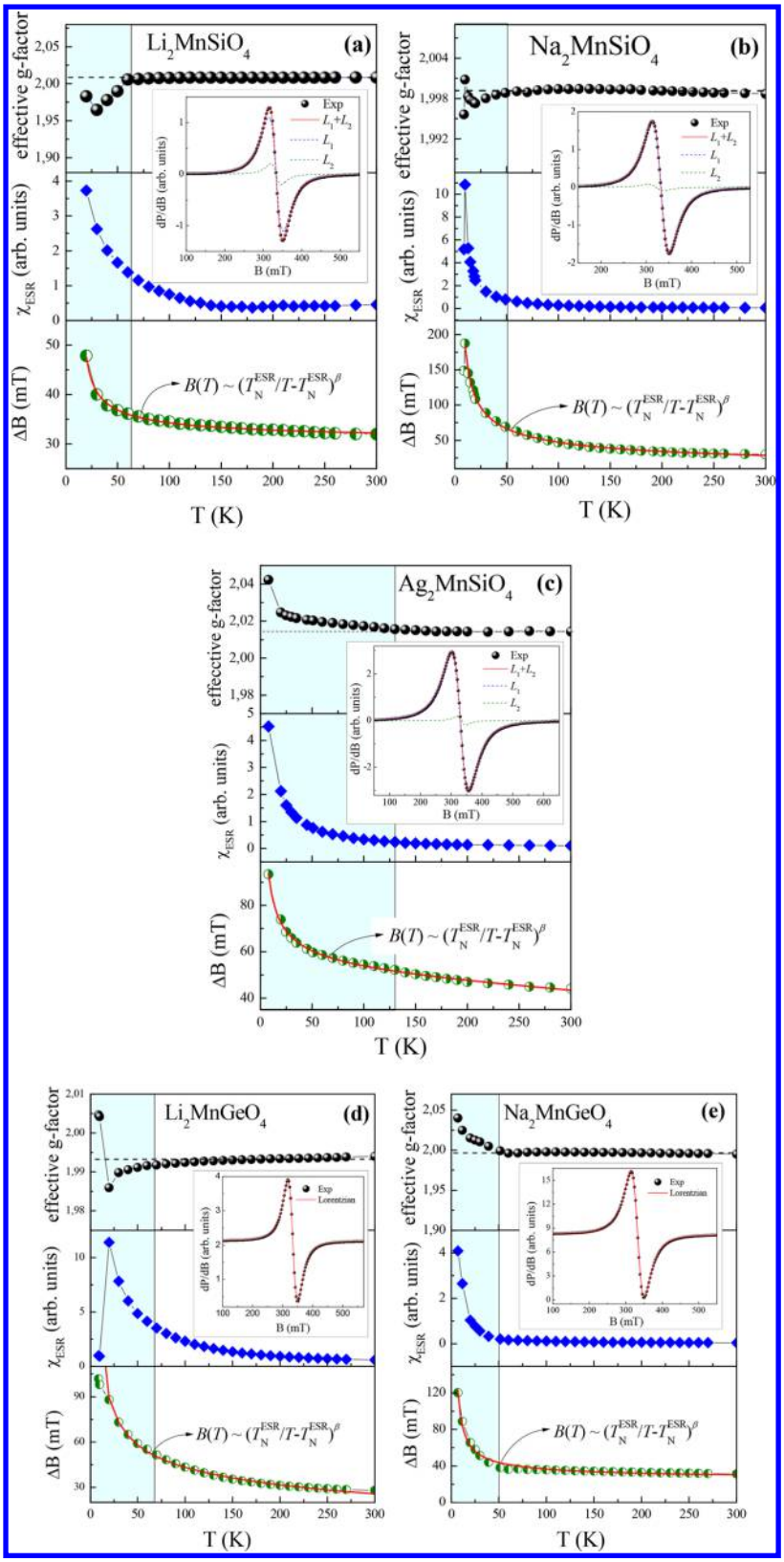

Figure 9. Temperature dependence of the effective *g*-factor (upper panels), the integral ESR intensity (middle panels), and the ESR line width (lower panels) of A_2MnXO_4. The red solid curves are the prediction from the Mori−Kawaski−Huber theory (see the text). Insets: Representative examples of ESR spectra fitting with two Lorentzians at (a) T = 250, (b) 230, and (c) 200 K, and with one Lorentzian at (d and e) T = 250 K. The black circles are experimental data; the blue and green curves are resolved components, and the red solid curve is their sum. The light blue regions show the temperature range where the presence of short-range correlations is obvious from the deviation of the *g*-value.

DOI: 10.1021/acs.inorgchem.7b02130
Inorg. Chem. 2017, 56, 14023−14039

$$\frac{dP}{dB} \propto \frac{d}{dB}\left[\frac{\Delta B}{\Delta B^2 + (B - B_r)^2} + \frac{\Delta B}{\Delta B^2 + (B + B_r)^2}\right] \quad (4)$$

where P is the power absorbed in the ESR experiment, B the magnetic field, B_r the resonance field, and ΔB the line width.

The parameters of the main resonance mode L_1 deduced from the fitting are collected in Figure 9 for all samples. The overall temperature behavior of the ESR parameters corroborates well with that of the static magnetic properties for all samples. The integral ESR intensity χ_{esr}, which is proportional to the number of magnetic spins, was estimated by double integration of the first derivative ESR spectrum dP/dB. The χ_{esr} follows the Curie–Weiss relationship and agrees with the behavior of the magnetic susceptibility χ. The parameters for A_2MnXO_4 (A = Li, Na) that undergo a long-range AFM order above 2 K exhibit anomalies in the vicinity of T_N. With decreasing temperature below ~100 K, the absorption line broadens markedly and passes through a maximum at about T_N. The effective g-factor remains almost temperature-independent down to 50–70 K for different samples ($g \approx 2$ for all samples) (see also Table 3). When the temperature decreases further, the g-factor deviates markedly from its high-temperature value. This indicates an increasing role of the short-range correlations upon approaching an order–disorder transition from above. It should be stressed that the value $g = 2.003$ at $T = 5$K reported for Li_2MnSiO_4 ($Pmn2_1$) by Belharouak et al.[6] from X-band ESR measurements does not reflect the paramagnetic (spectroscopic) g-factor because it was determined well below $T_N = 12$ K (i.e., in the long-range AFM-ordered state), where the resonance reflects collective excitations or, if probing the impurity spins, are affected by the internal exchange and anisotropy fields of the AFM phase.

The effective g-factor and the ESR line width demonstrate a more complicated behavior for Na_2MnGeO_4, and an additional anomaly around T^* can be seen. Below T^*, the description for the line shape of the experimental ESR spectra requires the use of two Lorentzians. Thus, similarly to thermodynamic data, the ESR data indicate the presence of impurity, most probably Mn_3O_4. The ESR parameters for Ag_2MnSiO_4 are similar to those of other A_2MnXO_4 (A = Li, Na; X = Si, Ge) but show greater short-range correlation effects in an essentially wider temperature range (i.e., at $T < 130$ K) and do not show any nonmonotonous behavior. This is consistent with the absence of a long-range AFM order within the temperature range studied, and the finding for short-range correlations confirms the result of the magnetization analysis.

The broadening of the ESR line upon approaching T_N may be treated in terms of a critical behavior of the ESR line width, which is caused by the slowing of spin fluctuations in the vicinity of an order–disorder transition.[68−71] This causes the divergence of the spin correlation length, which in turn affects the spin–spin relaxation time of exchange-narrowed ESR lines resulting in the critical broadening:

$$\Delta B(T) = \Delta B^* + A\left[\frac{T_N^{ESR}}{T - T_N^{ESR}}\right]^{\beta} \quad (5)$$

where the first term ΔB^* describes the exchange-narrowed line width, which is temperature-independent. The second term describes the critical behavior with T_N^{ESR} as the temperature of the order–disorder transition and β as the critical exponent. To account for the ΔB behavior of Ag_2MnSiO_4 over the high temperature range, it is necessary to include an additional third linear term into this fitting formula. The solid red curves on the lower panels of Figure 9 represent a least-squares fitting of the $\Delta B(T)$ experimental data using eq 5. The best fitting was obtained with the parameters listed in Table 5. The value of

Table 5. Fitting Parameters for the Temperature Dependence of the ESR Line Width ΔB for A_2MnXO_4 in Accordance with Eq 5

	T_N^{ESR} (K)	ΔB^* (mT)	β
Li_2MnSiO_4	13.3 ± 0.5	30 ± 1	0.55 ± 0.05
Na_2MnSiO_4	4.6 ± 0.5	4 ± 1	0.50 ± 0.05
Ag_2MnSiO_4	0.01 ± 0.01	48 ± 1	0.66 ± 0.05
Li_2MnGeO_4	6.5 ± 0.5	2 ± 1	0.37 ± 0.05
Na_2MnGeO_4	3.1 ± 0.5	24 ± 1	0.65 ± 0.05

T_N^{ESR} is in a reasonable agreement with the T_N obtained from the static magnetic susceptibility measurements. The critical exponents β for A_2MnSiO_4 (A = Li, Na, Ag) and Na_2MnGeO_4 vary in the range of 0.55–0.66 except for Li_2MnGeO_4, where $\beta = 0.37 \pm 0.05$ (Table 5). The theoretical β value expected for 3D Heisenberg antiferromagnets is $^1/_3$. This indicates either a low-dimensional or frustrated character of magnetism for A_2MnSiO_4 (A = Li, Na, Ag) and Na_2MnGeO_4.

3.7. Magnetic Phase Diagrams. By summarizing the anomalies observed from the field and temperature dependencies of the magnetization in the present work, we constructed the magnetic phase diagrams for A_2MnXO_4 (Figure 10). The phases A_2MnGeO_4 and A_2MnSiO_4 (A = Li, Na) have a long-range AFM ordered ground state. The weak magnetic anisotropy of the Mn^{2+} ($S = ^5/_2$) ions leads to spin-flop transitions at rather low magnetic fields, i.e., at around 2 T in compounds studied. Accordingly, the associated anisotropy gap is of the order of $\Delta \approx g\mu_B B_{SF}$ ($T = 0$) ≈ 0.23 meV. An additional anomaly B_{C1} in Na_2MnGeO_4 is related most probably to the presence of a small Mn_3O_4 impurity in the sample, as already mentioned.

3.8. Analyses of the Magnetic Properties in Terms of Spin Exchanges. In this section, we discuss the magnetic properties of A_2MnSiO_4 (A = Li, Na, Ag) and A_2MnGeO_4 (A = Li, Na) on the basis of their spin exchange interactions, which we evaluate by performing the energy-mapping analysis based on DFT calculations.[36,37]

3.8.1. Computational Details. We carried out spin-polarized DFT calculations using a (2a, b, 2c) supercell for Li_2MnSiO_4 and a (2a, 2b, 2c) supercell for Na_2MnSiO_4, $AgMnSiO_4$, Li_2MnGeO_4, and Na_2MnGeO_4 by employing the projected augmented wave method encoded in the Vienna Ab Initio Simulation Package (VASP)[72−74] with the generalized gradient approximation of Perdew, Burke, and Ernzerhof[75] for the exchange-correlation functionals with a plane wave cutoff energy of 520 eV, a set of 2 × 2 × 2 k-points, and a threshold 10^{-6} eV for energy convergence. The DFT plus on-site repulsion U (DFT+U) method[76] was employed at $U_{eff} = U - J = 3$, 4, and 5 eV to describe the electron correlation in the Mn 3d states.

For Li_2MnSiO_4, Na_2MnSiO_4, $AgMnSiO_4$, Li_2MnGeO_4, and Na_2MnGeO_4, we considered various spin exchange paths described in Tables 6–10. To extract the values of N spin exchanges, we examined the relative energies of the $N + 1$ ordered spin arrangements presented in Figures S1–S5 of the Supporting Information on the basis of DFT+U calculations

DOI: 10.1021/acs.inorgchem.7b02130
Inorg. Chem. 2017, 56, 14023−14039

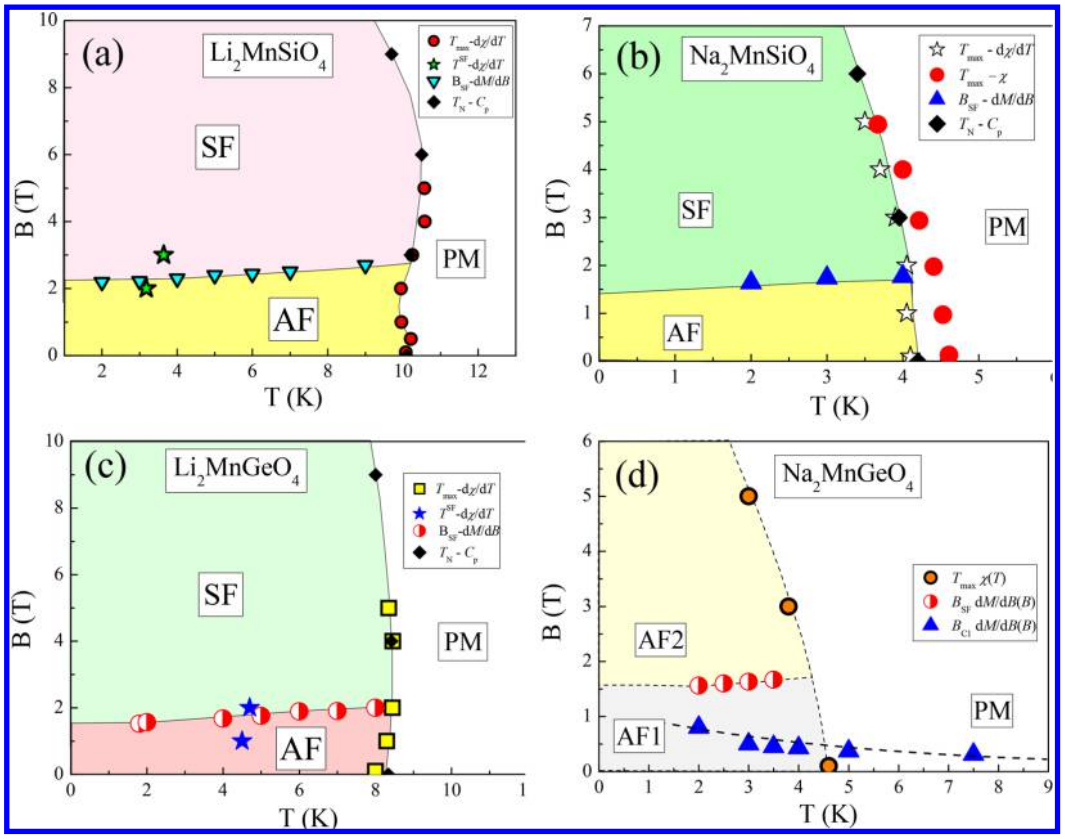

Figure 10. $B-T$ magnetic phase diagrams for (a) Li_2MnSiO_4, (b) Na_2MnSiO_4, (c) Li_2MnGeO_4, and (d) Na_2MnGeO_4.

Table 6. Geometrical Parameters Associated with the Spin Exchange Paths of Li_2MnSiO_4 and Their Values (in k_B K) Obtained from the DFT+U Calculations with U_{eff} = 4 eV[a]

	Mn···Mn (Å)	Mn−O (Å)	O···O (Å)	value (k_B K)
J_1 (white)	4.142	2.023, 2.091	2.723	−0.22
J_2 (yellow)	4.423	2.023, 2.091	2.698	−0.46
J_3 (purple)	4.485	2.023, 2.012	2.704	−0.29
J_4 (cyan)	4.742	2.023, 2.012	2.734	−0.86
J_5 (green)	5.073 (‖c)	2.091, 2.012	2.665	−3.24
J_6	6.305	2.012, 2.023	3.295	−0.03
J_7	6.336 (‖a)	2.012, 2.023	3.220	−0.01
J_8 (orange)	6.359	2.023, 2.023	2.679	−0.49

[a]The colors in the first column refer to those in Figure 11.

with U_{eff} = 3, 4, and 5 eV. The total spin exchange energy per supercell, E_{SE}, of each ordered spin arrangement is expressed as

$$E_{SE} = (n_1J_1 + n_2J_2 + n_3J_3 + \cdots + n_{N+}J_{N+1})S^2 \quad (6)$$

where S is the total spin on Mn^{2+} ($S = {}^5/_2$). From these expressions, we obtain N relative energies ΔE_{SE}. The N relative energies ΔE_{DFT} per supercell, calculated for the $N + 1$ ordered spin states by DFT+U calculations, and the values of $n_1 - n_{N+1}$ for each ordered spin arrangement are summarized in Tables S5−S14 of the Supporting Information. The values of $J_1 - J_N$, obtained by mapping the energies ΔE_{SE} onto ΔE_{DFT}, are summarized in Tables S15−S19 of the Supporting Information. In general, the calculated spin exchange constants are very weak; only a few have values greater than 1 K.

In the mean-field theory approximation,[77,78] the Curie−Weiss temperature, θ, is related to the spin exchange parameters as follows:

$$\theta = \left(\frac{S(S+1)}{3k_B}\right)\sum_i z_iJ_i \quad (7)$$

where z_i is the number of the nearest neighbors interacting along the exchange paths J_i (Table S20 of the Supporting Information), and $S = {}^5/_2$ for Mn^{2+}. The calculated values θ_{cal} obtained from the DFT+U calculations with U_{eff} = 4 eV are compared with the experimental ones θ_{exp} (Table 11 and Table S21 of the Supporting Information). The agreement between θ_{cal} and θ_{exp} is reasonably good, except for Na_2MnSiO_4, for which $\theta_{cal} \approx \theta_{exp}/2$. In what follows, we employ the spin exchanges $J_1 - J_{N+1}$ obtained from these calculations to discuss the observed magnetic properties of A_2MnXO_4. The values of $J_1 - J_{N+1}$ calculated by using U_{eff} = 4 eV and the geometrical parameters associated with these exchange paths are summarized in Tables 6−10.

3.8.2. Results. Li_2MnSiO_4. The arrangements of the spin exchange paths are depicted in Figure 11, where J_6 and J_7 are omitted because they are very weak. The remaining spin exchanges are all AFM with J_5 as the strongest one along the c-axis (hereafter along the ‖c-axis), and give rise to spin-frustrated triangles[59,79] (J_5, J_4, J_1), (J_5, J_2, J_3), (J_8, J_2, J_1), and (J_4, J_8, J_3) (Table 6). The most stable collinear spin arrangement deduced from these spin exchanges is illustrated in Figure 11, where the four strongest AFM exchanges J_5, J_4, J_8, and J_2 are coupled antiferromagnetically. Because J_1 and J_3 are considerably weaker than these four, the extent of spin frustration in the spin triangles is not strong, which accounts for the low spin frustration index f = 3.0.

Na_2MnSiO_4. The weakest exchange J_7 is neglected in our analysis. The exchanges J_1−J_6 are all AFM, with the largest one J_3 along the ‖c-axis (Figure 12). These AFM spin exchanges

DOI: 10.1021/acs.inorgchem.7b02130
Inorg. Chem. 2017, 56, 14023−14039

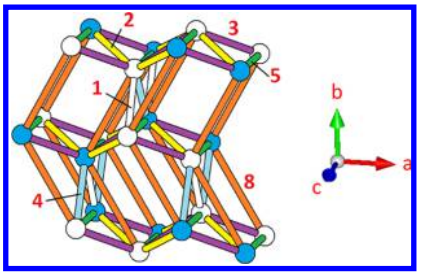

Figure 11. Spin exchange paths of the collinear spin arrangement expected for Li_2MnSiO_4, where the shaded and unshaded spheres represent up-spin and down-spin Mn^{2+} sites, respectively. The numbers 1, 2, etc. represent the spin exchanges J_1, J_2, etc., respectively.

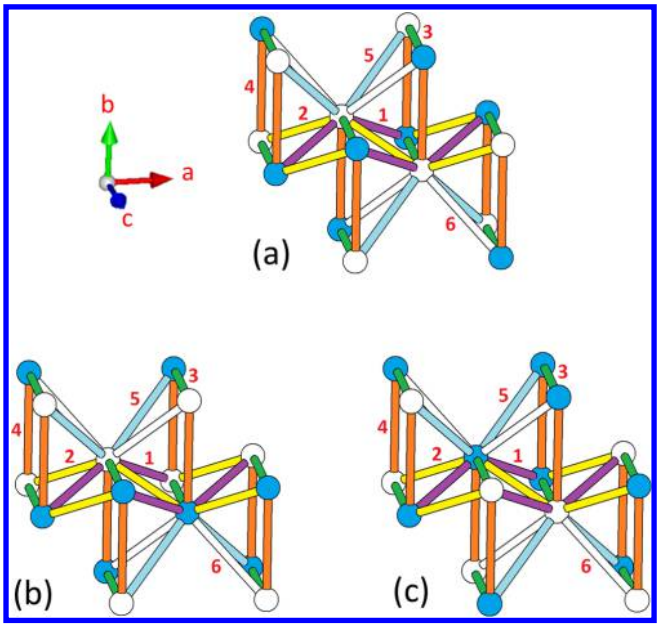

Figure 12. Spin exchange paths of the three low-energy collinear spin arrangements expected for Na_2MnSiO_4, where the shaded and unshaded spheres represent up-spin and down-spin Mn^{2+} sites, respectively. The numbers 1, 2, etc. represent the spin exchanges J_1, J_2, etc., respectively.

lead to spin-frustrated triangles (J_3, J_2, J_1), (J_3, J_6, J_5), (J_4, J_1, J_5), and (J_4, J_2, J_6) (Table 7). The three collinear spin arrangements depicted in Figure 12 are similar in energy. There is no dominant spin exchange interaction, and the extent in spin-frustrated triangle is significant triangle. This explains the high degree of spin frustration (f = 6.4).

Table 7. Geometrical Parameters Associated with the Spin Exchange Paths of Na_2MnSiO_4 and Their Values (in k_B K) Obtained from the DFT+U Calculations with U_{eff} = 4 eV[a]

path	Mn···Mn (Å)	Mn−O (Å)	O···O (Å)	value (k_B K)
J_1 (purple)	4.858	2.082, 2.079	2.652	−0.24
J_2 (yellow)	4.872	2.007, 2.079	2.687	−0.31
J_3 (green)	5.334 (‖c)	2.082, 2.007	2.644	−0.89
J_4 (orange)	5.610 (‖b)	2.079, 2.086	2.548	−0.38
J_5 (cyan)	5.662	2.082, 2.086	2.590	−0.20
J_6 (white)	5.674	2.086, 2.007	2.612	−0.27
J_7	7.029 (‖a)	2.007, 2.086	3.961	0.02

[a]The colors in the first column refer to those in Figure 12.

Ag_2MnSiO_4. J_2 is negligible compared with other spin exchanges. J_1 as well as J_3−J_6 are AFM, while J_7 is FM, with J_3 as the strongest exchange along the ‖c-axis (Table 8). These spin

Table 8. Geometrical Parameters Associated with the Spin Exchange Paths of Ag_2MnSiO_4 and Their Values (in k_B K) Obtained from the DFT+U Calculations with U_{eff} = 4 eV[a]

path	Mn···Mn (Å)	Mn−O (Å)	O···O (Å)	value (k_B K)
J_1 (yellow)	4.941	2.016, 2.111	2.653	−0.14
J_2	4.967	2.111, 1.962	2.720	−0.01
J_3 (green)	5.510 (‖c)	1.962, 2.016	2.737	−0.44
J_4 (white)	5.591	2.002, 2.016	2.630	−0.31
J_5 (cyan)	5.615	1.962, 2.002	2.767	−0.10
J_6 (orange)	5.648 (‖b)	2.111, 2.002	2.773	−0.14
J_7 (blue)	6.939 (‖a)	2.016, 2.002	3.927	0.17

[a]The colors in the first column refer to those in Figure 13a.

exchanges give rise to spin-frustrated triangles (J_3, J_4, J_5) and (J_4,J_1, J_6). In the most stable collinear spin arrangement deduced from these spin exchanges, depicted in Figure 13a, J_6 and J_3 have an AFM coupling, while J_7 has an FM coupling. Nevertheless, all spin exchanges are very weak, so effectively many different spin arrangements should have a similar energy. This would be responsible for why the spin-frustration index is high (f > 5).

Li_2MnGeO_4. The arrangements of the spin exchanges are shown in Figure 13b. J_1−J_5 are all AFM, with J_2 as the strongest one along the ‖c-axis. These AFM spin exchanges lead to spin-frustrated triangles (J_2, J_1, J_1), (J_2, J_3, J_3), (J_5, J_1, J_1), (J_3, J_1, J_4), and (J_5, J_3, J_3) (Table 9). The most stable collinear spin arrangement deduced from these spin exchanges is illustrated in Figure 13b, in which J_2, J_4, and J_5 have an AFM coupling, while the J_1 and J_3 paths have either an AFM or a FM coupling. J_2 is much stronger than J_1 and J_3; J_5 is stronger than J_1, and J_3 is stronger than J_1 and J_4. Thus, spin-frustration from the (J_2, J_1, J_1), (J_2, J_3, J_3), (J_5, J_1, J_1), and (J_3, J_1, J_4) is not strong. Only the spin exchanges in the (J_3, J_3, J_5) triangle are comparable in magnitude. This explains why the frustration is not large for Li_2MnGeO_4 (f = 3.5).

Na_2MnGeO_4. The arrangements of the spin exchanges are depicted in Figure 13c. The exchanges J_5 and J_7 are negligible compared with the rest. The strongest exchange J_3 is along the ‖c-axis. These AFM spin exchanges lead to spin-frustrated triangles (J_3, J_1, J_2) and (J_6, J_2, J_4) (Table 10). The most stable collinear spin arrangement deduced from these spin exchanges is depicted in Figure 13c. J_1 and J_2 are comparable in strength in the (J_3, J_1, J_2), while J_2 and J_4 are comparable in the triangle. This may explain why the spin-frustration index is high (f = 6.8).

3.9. General Remarks on Magnetic Properties. There are several points of importance to note when discussing the spin exchange interactions of A_2MnGeO_4 (A = Li, Na) and A_2MnSiO_4 (A = Li, Na, Ag):

(a) In all these phases, the most significant spin exchange runs along the ‖c-axis.
(b) The spin frustration in all of these phases can be attributed to the presence of spin-frustrated exchange triangles.
(c) Compared with those of A_2MnGeO_4 and A_2MnSiO_4 (A = Li, Na), all spin exchanges of Ag_2MnSiO_4 are very weak. This makes many different spin arrangements have a similar energy (i.e., highly spin frustrated) so that

DOI: 10.1021/acs.inorgchem.7b02130
Inorg. Chem. 2017, 56, 14023−14039

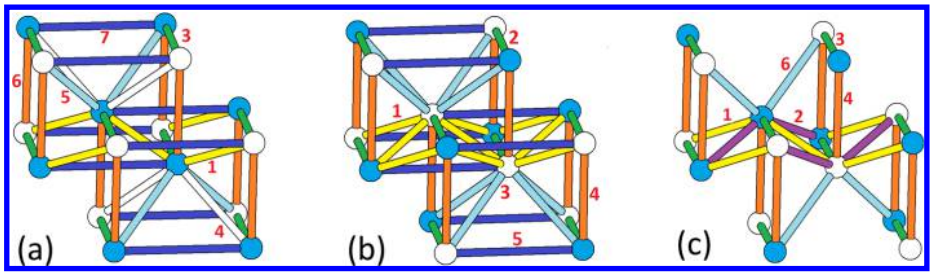

Figure 13. Spin exchange paths of the collinear spin arrangement expected for (a) Ag_2MnSiO_4, (b) Li_2MnGeO_4, and (c) Na_2MnGeO_4, where the shaded and unshaded spheres represent up-spin and down-spin Mn^{2+} sites, respectively. The coordinate axes used for presenting the Mn^{2+} ion arrangement are identical to those shown in Figure 12. The numbers 1, 2, etc. represent the spin exchanges J_1, J_2, etc., respectively.

Table 9. Geometrical Parameters Associated with the Spin Exchange Paths of Li_2MnGeO_4 and Their Values (in k_B K) Obtained from the DFT+U Calculations with U_{eff} = 4 eV[a]

path	Mn···Mn (Å)	Mn−O (Å)	O···O (Å)	value (k_B K)
J_1 (yellow)	4.518	2.052, 2.106	2.834	−0.23
J_2 (green)	5.054 (‖c)	2.156, 2.106	2.783	−2.37
J_3 (cyan)	5.450	2.052, 2.052	3.148	−0.50
J_4 (orange)	5.476 (‖b)	2.106, 2.052	3.190	−0.31
J_5 (blue)	6.468 (‖a)	2.052, 2.052	2.896	−0.48

[a]The colors in the first column refer to those in Figure. 13b.

Table 10. Geometrical Parameters Associated with the Spin Exchange Paths of Na_2MnGeO_4 and Their Values (in k_B K) Obtained from the DFT+U Calculations with U_{eff} = 4 eV[a]

path	Mn···Mn (Å)	Mn−O (Å)	O···O (Å)	value (k_B K)
J_1 (yellow)	4.905	1.892, 2.091	2.964	−0.51
J_2 (purple)	4.912	2.091, 1.840	2.984	−0.39
J_3 (green)	5.407 (‖c)	1.840, 1.892	3.160	−1.41
J_4 (orange)	5.730 (‖b)	2.091, 2.119	2.661	−0.31
J_5	5.840	2.119, 1.892	3.002	−0.04
J_6 (cyan)	5.846	1.840, 2.119	2.852	−1.10
J_7	7.164 (‖a)	1.892, 2.119	4.098	0.01

[a]The colors in the first column refer to those in Figure 13c.

Table 11. Calculated and Experimental Curie−Weiss Temperatures

system	calculated	experimental
Li_2MnSiO_4	−29.5	−30
Na_2MnSiO_4	−13.2	−27
Ag_2MnSiO_4	−5.7	−9
Li_2MnGeO_4	−26.9	−27
Na_2MnGeO_4	−21.8	−27

Ag_2MnSiO_4 does not undergo a long-range AFM ordering down to 2 K.

(d) If the index $f = \Theta/T_N > 5$, the system is considered to be frustrated and may not undergo a long-range AFM ordering.[59] Nevertheless, for the systems with $S > {}^1/_2$ and in the presence of different pathways for noticeable super-superexchange interactions, this naïve rule does not work, as we observed here for Na_2MnSiO_4 and Na_2MnGeO_4, which order although their f indices are greater than 6 (i.e., 6.4 and 6.8, respectively).

Aiming to get general view on common trends between the magnetic properties of the compounds under study, we plotted the Néel temperature versus several structurally related geometrical parameters for dominating exchange pathways. The results are summarized in Figure 14. In full agreement with the naïve expectations, the Néel temperature decreases with increasing both the average bond angle M−O−X and the M−M distance along the c-axis, which corresponds to dominating exchange interaction in A_2MXO_4 family (A = Li, Na, Ag; X = Si, Ge) (Figure 14a). This corroborates well the results obtained from the theoretical calculations. The strongest exchange integral $J_{c\text{-axis}}$ correlates with the T_N value, and their dependence has almost linear character (Figure 14b). The detailed magnetic investigation of the A_2MXO_4 highlights the crucial role of frustration. Our data show that, except for Ag_2MnSiO_4, which features only very weak magnetic interactions and must be omitted in this respect, the experimental values of the Weiss temperatures are very similar, i.e., about ∼30 K for all compounds studied (see Table 3). The experimental data hence imply that the sum of the exchange integrals, which is represented by the Weiss temperature Θ, does not change in the series. Accordingly, as well-known for frustrated magnetic systems, the actual onset of long-range magnetic order which, in contrast to Θ changes a lot in A_2MnXO_4, is determined by the strength of the thermal fluctuations and depends only to a minor degree on the value of the magnetic exchange. In the compounds under study, the increase of magnetic exchange along the c-axis is counterbalanced by the decrease in the perpendicular directions, but the frustration parameter changes from a rather moderate to an intermediate level. The series of compounds is a model illustrating the relationship of T_N and frustration without significant changes of the overall size of magnetic interaction (Figure 14b). Note that the isotropic nature of the Mn^{2+} ions assume the weak influence of magnetic anisotropy in the compounds under study. Our data hence enable studying how thermal fluctuations increase upon the increase of frustration in a rather classical $S = {}^5/_2$ Heisenberg system.

4. CONCLUSIONS

We prepared the four new phases A_2MnGeO_4(A = Li, Na) and A_2MnSiO_4 (A = Na, Ag), determined their crystal structures, and characterized the magnetic properties of these four phases and Li_2MnSiO_4 by magnetic susceptibility, specific heat, magnetization, and ESR measurements and also by evaluating their spin exchange constants. The magnetic susceptibility and specific heat data reveal that Ag_2MnSiO_4 remains paramagnetic down to 2 K, whereas phases A_2MnXO_4 (A = Li, Na; X = Si, Ge) undergo a 3D AFM ordering. The five phases A_2MnGeO_4 (A = Li, Na) and A_2MnSiO_4 (A = Li, Na, Ag) exhibit short-range AFM ordering correlations, indicating that they are low-dimensional magnetic materials. The magnetization isotherms indicate a magnetic field induced spin-reorientation (spin-flop

DOI: 10.1021/acs.inorgchem.7b02130
Inorg. Chem. 2017, 56, 14023−14039

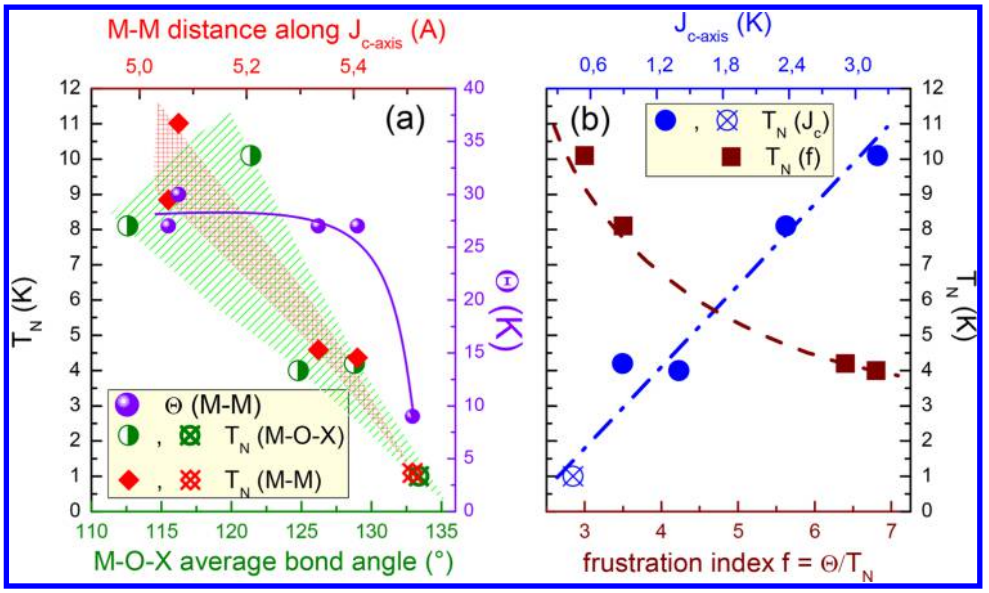

Figure 14. (a) Dependence of the Néel temperature T_N and the Weiss temperature Θ on average bond angle M−O−X and M−M distance along the *c*-axis, which corresponds to dominating exchange interaction in A_2MXO_4 family (A = Li, Na, Ag; X = Si, Ge). (b) Dependence of the Néel temperature T_N on spin frustration indexes and main exchange integrals in A_2MXO_4 family (A = Li, Na, Ag; X = Si, Ge).

type) transition at $T < T_N$ for all AFM phases. The spin-flop fields of about 2 T imply a small magnetic anisotropy gaps of Δ ≈ 0.23 meV. Summarizing the thermodynamic data in magnetic fields up to 9 T allows one to construct the magnetic phase diagrams of A_2MnXO_4 (A = Li, Na; X = Si, Ge). The magnetic properties of A_2MnGeO_4 (A = Li, Na) and A_2MnSiO_4 (A = Li, Na, Ag) experimentally determined are well-accounted for by their spin exchange constants evaluated by performing energy-mapping analysis.

■ ASSOCIATED CONTENT

Supporting Information

The Supporting Information is available free of charge on the ACS Publications website at DOI: 10.1021/acs.inorgchem.7b02130.

Supplementary Tables S1−S21: XRD data collection and refinement details for A_2MnXO_4; atomic coordinates and displacement parameters for A_2MnXO_4; lattice parameters of new A_2MnXO_4 in comparison with the literature data for their analogues; space groups and values of T_N, Θ and μ_{eff} of A_2MXO_4 (M = Fe, Co) from magnetic susceptibility measurements and *g*-factor of Li_2FeSiO_4 from ESR measurements; coefficients defining the total spin exchange energies of the ordered spin states per supercells of Li_2MnSiO_4, Na_2MnSiO_4, Ag_2MnSiO_4, Li_2MnGeO_4, and Na_2MnGeO_4; relative energies of the ordered spin states obtained from DFT+*U* calculations per supercells of Li_2MnSiO_4, Na_2MnSiO_4, Ag_2MnSiO_4, Li_2MnGeO_4, and Na_2MnGeO_4; values of the spin exchanges for Li_2MnSiO_4, Na_2MnSiO_4, Ag_2MnSiO_4, Li_2MnGeO_4, and Na_2MnGeO_4 determined from DFT +*U* calculations; coefficients z_1−z_8 defining the number of nearest neighbors connected by the spin exchange J_1−J_8; calculated and experimental Curie−Weiss temperatures; Supplementary Figures S1−S5: ordered spin states of Li_2MnSiO_4, Na_2MnSiO_4, Ag_2MnSiO_4, Li_2MnGeO_4, and Na_2MnGeO_4 (PDF)

Accession Codes

CCDC 1578951−1578954 contain the supplementary crystallographic data for this paper. These data can be obtained free of charge via www.ccdc.cam.ac.uk/data_request/cif, by emailing data_request@ccdc.cam.ac.uk, or by contacting The Cambridge Crystallographic Data Centre, 12 Union Road, Cambridge CB2 1EZ, UK; fax: +44 1223 336033.

■ AUTHOR INFORMATION

Corresponding Author

*E-mail: vbn@sfedu.ru.

ORCID

Vladimir B. Nalbandyan: 0000-0002-8624-0165

Myung-Hwan Whangbo: 0000-0002-2220-1124

Notes

The authors declare no competing financial interest.

■ ACKNOWLEDGMENTS

V.B.N., E.A.Z., and I.L.S. are thankful to the Russian Foundation for Basic Research for Grant 14-03-01122. Preparation and preliminary XRD identification of the phases by V.V.P., V.B.N., and A.A.P. was supported by Russian Federal program "Integration" (Project N0674), Grant-in-Aid 00-15 from the International Centre for Diffraction Data and Internal Grant K-07-T-20 from the SFU. The authors thank Dr. S. N. Polyakov for his help with the XRD data collection. Measurement and interpretation of the XPS data by Drs. K. I. Maslakov, S. V. Savilov, and I. V. Morozov is also gratefully acknowledged. The work at NCSU used resources of the HPC at NCSU as well as the NERSC Centre, a DOE Office of Science User Facility supported by the Office of Science of the U.S. Department of Energy under Contract DE-AC02-05CH11231. This work was supported in part by the Ministry of Education and Science of the Russian Federation in the framework of Increase Competitiveness Program of NUST MISiS K2-2017-005, and by Act 211 of Government of the Russian Federation, Contracts 02.A03.21.0004 and 02.A03.21.0011. E.A.Z. acknowledges support from the Russian

DOI: 10.1021/acs.inorgchem.7b02130
Inorg. Chem. 2017, 56, 14023−14039

Foundation for Basic Research through Grant 17-52-45014 and the Russian Science Foundation through Project 17-12-01207.

REFERENCES

(1) Nyten, A.; Abouimrane, A.; Armand, M.; Gustafsson, T.; Thomas, J. O. Electrochemical performance of Li_2FeSiO_4 as a new Li-battery cathode material. *Electrochem. Commun.* **2005**, *7*, 156−160.

(2) Dominko, R.; Bele, M.; Gaberšček, M.; Meden, A.; Remškar, M.; Jamnik, J. Structure and electrochemical performance of Li_2MnSiO_4 and Li_2FeSiO_4 as potential Li-battery cathode materials. *Electrochem. Commun.* **2006**, *8*, 217−222.

(3) Zaghib, K.; Salah, A. A.; Ravet, N.; Mauger, A.; Gendron, F.; Julien, C. M. Structural, magnetic and electrochemical properties of lithium iron orthosilicate. *J. Power Sources* **2006**, *160*, 1381−1386.

(4) Politaev, V. V.; Petrenko, A. A.; Nalbandyan, V. B.; Medvedev, B. S.; Shvetsova, E. S. Crystal structure, phase relations and electrochemical properties of monoclinic Li_2MnSiO_4. *J. Solid State Chem.* **2007**, *180*, 1045−1050.

(5) Lyness, C.; Delobel, B.; Armstrong, A. R.; Bruce, P. G. The lithium intercalation compound Li_2CoSiO_4 and its behavior as a positive electrode for lithium batteries. *Chem. Commun.* **2007**, 4890−4892.

(6) Belharouak, I.; Abouimrane, A.; Amine, K. Structural and Electrochemical Characterization of Li_2MnSiO_4 Cathode Material. *J. Phys. Chem. C* **2009**, *113*, 20733−20737.

(7) Gong, Z.; Yang, Y. Recent advances in the research of polyanion-type cathode materials for Li-ion batteries. *Energy Environ. Sci.* **2011**, *4*, 3223−3242.

(8) Girish, H.-N.; Shao, G.-Q. Advances in high-capacity Li_2MSiO_4 (M = Mn, Fe, Co, Ni···) cathode materials for lithium-ion batteries. *RSC Adv.* **2015**, *5*, 98666−98686.

(9) (a) Gummow, R. J. In *Nanomaterials in Advanced Batteries and Supercapacitors*; Ozoemena, K. I., Chen, S., Eds.; Springer International Publishing: Switzerland, 2016; Chapter 2, pp 25−54. (b) Billaud, J.; Eames, C.; Tapia-Ruiz, N.; Roberts, M. R.; Naylor, A. J.; Armstrong, A. R.; Islam, M. S.; Bruce, P. G. Evidence of Enhanced Ion Transport in Li-Rich Silicate Intercalation Materials. *Adv. Energy Mater.* **2017**, *7*, 1601043. (c) Li, W.; Song, B.; Manthiram, A. High-voltage positive electrode materials for lithium-ion batteries. *Chem. Soc. Rev.* **2017**, *46*, 3006−3059. (d) Cheng, Q.; He, W.; Zhang, X.; Li, M.; Wang, L. Modification of Li_2MnSiO_4 cathode materials for lithium-ion batteries: a review. *J. Mater. Chem. A* **2017**, *5*, 10772−10797.

(10) Duncan, H.; Kondamreddy, A.; Mercier, P. H. J.; Le Page, Y.; Abu-Lebdeh, Y.; Couillard, M.; Whitfield, P. S.; Davidson, I. J. Novel Pn Polymorph for Li_2MnSiO_4 and Its Electrochemical Activity As a Cathode Material in Li-Ion Batteries. *Chem. Mater.* **2011**, *23*, 5446−5456.

(11) Aravindan, V.; Karthikeyan, K.; Ravi, S.; Amaresh, S.; Kim, W. S.; Lee, Y. S. Adipic acid assisted sol-gel synthesis of Li_2MnSiO_4 nanoparticles with improved lithium storage properties. *J. Mater. Chem.* **2010**, *20*, 7340−7343.

(12) Zhang, Y.; Yu, H.; Zhou, H. Two-electron migration orthosilicate cathode materials for Na-ion batteries. *J. Mater. Chem. A* **2014**, *2*, 11574−11577.

(13) Chen, C.-Y.; Matsumoto, K.; Nohira, T.; Hagiwara, R. Na_2MnSiO_4 as a positive electrode material for sodium secondary batteries using an ionic liquid electrolyte. *Electrochem. Commun.* **2014**, *45*, 63−66.

(14) (a) Li, S.; Guo, J.; Ye, Z.; Zhao, X.; Wu, S.; Mi, J.-X.; Wang, C.-Z.; Gong, Z.; McDonald, M. J.; Zhu, Z.; Ho, K.-M.; Yang, Y. Zero-Strain Na_2FeSiO_4 as Novel Cathode Material for Sodium-Ion Batteries. *ACS Appl. Mater. Interfaces* **2016**, *8*, 17233−17238. (b) Treacher, J.; Wood, S. M.; Islam, M. S.; Kendrick, E. Na_2CoSiO_4 as a cathode material for sodium-ion batteries: structure, electrochemistry and diffusion pathways. *Phys. Chem. Chem. Phys.* **2016**, *18*, 32744. (c) Bianchini, F.; Fjellvag, H.; Vajeeston, P. First-principles study of the structural stability and electrochemical properties of Na_2MSiO_4 (M = Mn, Fe, Co and Ni) polymorphs. *Phys. Chem. Chem. Phys.* **2017**, *19*, 14462−14470.

(15) (a) Gao, S.; Zhao, J.; Zhao, Y.; Wu, Y.; Zhang, X.; Wang, L.; Liu, X.; Rui, Y.; Xu, J. Na_2CoSiO_4 as a novel positive electrode material for sodium-ion capacitors. *Mater. Lett.* **2015**, *158*, 300−303. (b) Xia, N.; Zhao, J.; Lai, C.; Wang, H.; Gao, S.; Zhang, Z.; Xu, J. Electrochemical performances of Na_2MnSiO_4 as an energy storage material in sodium-ion capacitors. *J. Appl. Electrochem.* **2017**, *47*, 343−349.

(16) (a) Li, X.; Ouyang, S.; Kikugawa, N.; Ye, J. Novel Ag_2ZnGeO_4 photocatalyst for dye degradation under visible light irradiation. *Appl. Catal., A* **2008**, *334*, 51−58. (b) Zhang, N.; Ouyang, S.; Kako, T.; Ye, J. Synthesis of hierarchical Ag_2ZnGeO_4 hollow spheres for enhanced photocatalytic property. *Chem. Commun.* **2012**, *48*, 9894−9896.

(17) Liu, J.; Zhang, G. Facile synthesis and enhanced visible-light photocatalytic activity of micro/nanostructured Ag_2ZnGeO_4 hollow spheres. *Mater. Sci. Eng., B* **2015**, *193*, 198−205.

(18) McDonald, K. J.; Zhang, R.; Ling, C.; Zhou, L. Q.; Zhang, R.; Whittingham, M. S.; Jia, H. Hydrothermal synthesis, structure refinement, and electrochemical characterization of Li_2CoGeO_4 as an oxygen evolution catalyst. *J. Mater. Chem. A* **2014**, *2*, 18428−18434.

(19) Baur, W. H.; Ohta, T.; Shannon, R. D. Structure of magnesium disodium silicate Na_2MgSiO_4 and ionic conductivity in tetrahedral structures. *Acta Crystallogr., Sect. B: Struct. Crystallogr. Cryst. Chem.* **1981**, *37*, 1483−1491.

(20) Delmas, C.; Maazaz, A.; Hagenmuller, P. Crystal Chemistry and Fast Ionic Conductivity of Sodium and Potassium Phases Having Cristobalite-Related structures. *Solid State Ionics* **1983**, *9−10*, 83−88.

(21) Grins, J. Ionic conductivities in compounds based on chemical substitutions in Na_2ZnSiO_4. *Solid State Ionics* **1986**, *18−19*, 577−581.

(22) Frostäng, S.; Grins, J.; Nygren, M. Ionic Conductivity Studies and Phase Analysis of the Na_2BeSiO_4-$Na_2BeSi_2O_6$ System. *J. Solid State Chem.* **1988**, *72*, 92−99.

(23) Grins, J. Structure and Ionic Conductivity of Na_2BeGeO_4. *J. Solid State Chem.* **1995**, *118*, 62−65.

(24) Vaivars, G.; Grins, J.; Hörlin, T. Synthesis, structure and conductivity of Ag_2ZnSiO_4, Ag_2ZnGeO_4 and Ag_2BeSiO_4. *Solid State Ionics* **1995**, *78*, 259−267.

(25) Arkhangel'skii, G. E.; L'vova, E.; Fok, M. V. Luminescence of manganese in sodium zincogermanate crystals. *J. Appl. Spectrosc.* **1971**, *14*, 77−80.

(26) Jousseaume, C.; Kahn-Harari, A.; Vivien, D.; Derouet, J.; Ribot, F.; Villain, F. Structural and spectroscopic characterization of Cr:Li_2MgSiO_4 (γ_0). *J. Mater. Chem.* **2002**, *12*, 1525−1529.

(27) Jin, Y.; Hu, Y.; Duan, H.; Chen, L.; Wang, X. The long persistent luminescence properties of phosphors: Li_2ZnGeO_4 and Li_2ZnGeO_4:Mn^{2+}. *RSC Adv.* **2014**, *4*, 11360−11366.

(28) Wang, T.; Bian, W.; Zhou, D.; Qiu, J.; Yu, X.; Xu, X. Tunable LLP via Energy Transfer between $Na_{2-y}(Zn_{1-x}Ga_x)GeO_4$ Sosoloid Host and Emission Centers with the Assistance of Zn Vacancies. *J. Phys. Chem. C* **2015**, *119*, 14047−14055.

(29) Jin, Y.; Hu, Y.; Fu, Y.; Ju, G.; Mu, Z.; Chen, R.; Lin, J.; Wang, Z. Preparation, Design, and Characterization of the Novel Long Persistent Phosphors: Na_2ZnGeO_4 and Na_2ZnGeO_4:Mn^{2+}. *J. Am. Ceram. Soc.* **2015**, *98*, 1555−1561.

(30) Wintenberger, M. Ordre magnetique dans Li_2CoGeO_4, Na_2CoGeO_4 et Na_2CoSiO_4. *Compt. Rend. Acad. Sci.* **1970**, *271*, 669−672.

(31) Wintenberger, M.; Lambert-Andron, B. Structures magnetiques de Na_2CoSiO_4 et Na_2CoGeO_4. *phys. stat. sol. (a)* **1973**, *18*, 209−213.

(32) Bini, M.; Ferrari, S.; Ferrara, C.; Mozzati, M. C.; Capsoni, D.; Pell, A. J.; Pintacuda, G.; Canton, P.; Mustarelli, P. Polymorphism and magnetic properties of Li_2MSiO_4 (M = Fe, Mn) cathode materials. *Sci. Rep.* **2013**, *3*, 3452.

(33) Avdeev, M.; Mohamed, Z.; Ling, C. D. Magnetic structures of β_I-Li_2CoSiO_4 and γ_0-Li_2MnSiO_4: crystal structure type vs. magnetic topology. *J. Solid State Chem.* **2014**, *216*, 42−48.

(34) McClune, W. F., Ed. *Powder Diffraction File*; ICDD: Newtown Square Pennsylvania, United States, 2006; patterns 00-55-638, 00-55-699, 00-55-704, 00-56-94, 00-56-298.

DOI: 10.1021/acs.inorgchem.7b02130
Inorg. Chem. 2017, 56, 14023−14039

(35) Tarte, P.; Cahay, R. Synthese et structure d'une nouvelle familie de composes $Li_2X^{II}SiO_4$ et $Li_2X^{II}GeO_4$ structuralement apparentes a Li_3PO_4. *Compt. Rend. Acad. Sci.* **1970**, *271*, 777−779.
(36) Whangbo, M.-H.; Koo, H.-J.; Dai, D. Spin exchange interactions and magnetic structures of extended magnetic solids with localized spins: theoretical descriptions on formal, quantitative and qualitative levels. *J. Solid State Chem.* **2003**, *176*, 417−481.
(37) Xiang, H. J.; Lee, C.; Koo, H.-J.; Gong, X. G.; Whangbo, M.-H. Magnetic properties and energy-mapping analysis. *Dalton Trans.* **2013**, *42*, 823−853.
(38) Koryakina, N. S.; Suvorova, N. V.; Dem'yanets, L. N.; Maksimov, B. A.; Ilyukhin, V. V.; Belov, N. V. Crystallization of Germanates in the System Li_2O-CdO-GeO_2-H_2O and the Crystal Structure of Li, Cd Orthogermanate. *Soviet Physics Doklady* **1971**, *16*, 700−703.
(39) Joubert-Bettan, C. A.; Lachenal, R.; Bertaut, E. F.; Parthe, E. The Crystal Structures of Na_2ZnSiO_4, Na_2ZnGeO_4, and Na_2MgGeO_4. *J. Solid State Chem.* **1969**, *4*, l−5.
(40) Plakhov, G. F.; Belov, N. V. Crystal structures of $Na_2Zn[SiO_4]$ and $Na_2Be[SiO_4]$, refined with allowance for thermal vibration anisotropy of the atoms. *Kristallografiya* **1979**, *24*, 1177−1183.
(41) Larson, A. C.; Von Dreele, R. B. *General Structure Analysis System (GSAS); Los Alamos National Laboratory Report LAUR 86-748*; Los Alamos National Laboratory, Los Alamos, NM, United States, 2004.
(42) Toby, B. H. EXPGUI, a graphical user interface for GSAS. *J. Appl. Crystallogr.* **2001**, *34*, 210−213.
(43) Shannon, R. D. Revised Effective Ionic Radii and Systematic Studies of Interatomic Distances in Halides and Chalcogenides. *Acta Crystallogr., Sect. A: Cryst. Phys., Diffr., Theor. Gen. Crystallogr.* **1976**, *32*, 751−767.
(44) O'Keeffe, M. On the arrangements of ions in crystals. *Acta Crystallogr., Sect. A: Cryst. Phys., Diffr., Theor. Gen. Crystallogr.* **1977**, *33*, 924−927.
(45) Avdeev, M.; Nalbandyan, V. B.; Shukaev, I. L. Alkali Metal Cation and Proton Conductors: Relationships between Composition, Crystal Structure, and Properties. In *Solid State Electrochemistry: Fundamentals, Methodology and Applications*; Kharton, V. V., Ed.; Wiley-VCH: Weinheim, 2009, pp 227−278.
(46) Langlet, G. Structure de monoaluminate de cesium. *Compt. Rend. Acad. Sci.* **1964**, *259*, 3769−3770.
(47) (a) Ali, N. Z.; Nuss, J.; Sheptyakov, D.; Jansen, M. The $AFeO_2$ (A = K, Rb and Cs) family: A comparative study of structures and structural phase transitions. *J. Solid State Chem.* **2010**, *183*, 752−759. (b) Sheptyakov, D.; Ali, N. Z.; Jansen, M. A neutron diffraction study of structural and magnetic transformations in $AFeO_2$ (A = K, Rb and Cs). *J. Phys.: Condens. Matter* **2010**, *22*, 426001.
(48) Plattner, E.; Vollenke, H.; Wittmann, A. Die Kristallstruktur der Verbindung Li_2ZnGeO_4. *Monatsh. Chem.* **1976**, *107*, 921−927.
(49) Marezio, M. The crystal structure of $LiGaO_2$. *Acta Crystallogr.* **1965**, *18*, 481−484.
(50) Yang, Z.; Ding, K.; Miyawaki, R.; Li, H. Reinvestigation of the crystal structure of liberite, Li_2BeSiO_4. *Neues Jahrb. Mineral., Abh.* **2014**, *191*, 311−316.
(51) Maksimov, B. A.; Ilyukhin, V. V.; Belov, N. V. Crystal structure of Na_2CoGeO_4 orthogermanate. *Dokl. Akad. Nauk SSSR* **1978**, *242*, 1070−1073.
(52) Müller, H.-P.; Hoppe, R. Zur Kristallstruktur von $KGaO_2$ und $NaGaO_2$. *Z. Anorg. Allg. Chem.* **1992**, *611*, 73−80.
(53) Nagatani, H.; Suzuki, I.; Kita, M.; Tanaka, M.; Katsuya, Y.; Sakata, O.; Omata, T. Structure of β-$AgGaO_2$; ternary I-III-VI_2 oxide semiconductor with a wurtzite-derived structure. *J. Solid State Chem.* **2015**, *222*, 66−70.
(54) Kaduk, J. A.; Pei, S. The Crystal Structure of Hydrated Sodium Aluminate, $NaAlO_2 \cdot 5/4H_2O$, and Its Dehydration Product. *J. Solid State Chem.* **1995**, *115*, 126−139.
(55) Li, J.; Sleight, A. W. Structure of β-$AgAlO_2$ and structural systematics of tetrahedral MM'X_2 compounds. *J. Solid State Chem.* **2004**, *177*, 889−894.
(56) Carlin, R. L. *Magnetochemistry*; Springer-Verlag: Berlin, Heidelberg, New York, Tokyo, 1986.
(57) Peets, D. C.; Sim, H.; Choi, S.; Avdeev, M.; Lee, S.; Kim, S. J.; Kang, H.; Ahn, D.; Park, J.-G. Magnetic transitions in the chiral armchair-kagome system $Mn_2Sb_2O_7$. *Phys. Rev. B: Condens. Matter Mater. Phys.* **2017**, *95*, 014424.
(58) Bain, G. A.; Berry, J. F. Diamagnetic Corrections and Pascal's Constants. *J. Chem. Educ.* **2008**, *85*, 532−536.
(59) Greedan, J. E. Geometrically frustrated magnetic materials. *J. Mater. Chem.* **2001**, *11*, 37−53.
(60) Wu, S. Q.; Zhu, Z. Z.; Yang, Y.; Hou, Z. F. Structural stabilities, electronic structures and lithium deintercalation in Li_xMSiO_4 (M = Mn, Fe, Co, Ni): A GGA and GGA + *U* study. *Comput. Mater. Sci.* **2009**, *44*, 1243−1251.
(61) Zhong, G.; Li, Y.; Yan, P.; Liu, Z.; Xie, M.; Lin, H. Structural, Electronic, and Electrochemical Properties of Cathode Materials Li_2MSiO_4 (M = Mn, Fe, and Co): Density Functional Calculations. *J. Phys. Chem. C* **2010**, *114*, 3693−3700.
(62) Zhang, P.; Zheng, Y.; Wu, S. Q.; Zhu, Z. Z.; Yang, Y. Hybrid density functional investigations of Li_2MSiO_4 (M = Mn, Fe and Co) cathode materials. *Comput. Mater. Sci.* **2014**, *83*, 45−50.
(63) Larsson, P.; Ahuja, R.; Nyten, A.; Thomas, J. O. An ab initio study of the Li-ion battery cathode material Li_2FeSiO_4. *Electrochem. Commun.* **2006**, *8*, 797−800.
(64) Kalantarian, M. M.; Asgari, S.; Mustarelli, P. Theoretical investigation of Li_2MnSiO_4 as a cathode material for Li-ion batteries: a DFT study. *J. Mater. Chem. A* **2013**, *1*, 2847−2855.
(65) Tari, A. *The specific heat of matter at low temperature*; Imperial College Press: London, 2003.
(66) Losee, D. B.; McElearney, J. N.; Shankle, G. E.; Carlin, R. L.; Cresswell, P. J.; Robinson, W. T. An Anisotropic Low-Dimensional Ising System, $[(CH_3)_3NH]CoCl_3 \cdot 2H_2O$: Its Structure and Canted Antiferromagnetic Behavior. *Phys. Rev. B* **1973**, *8*, 2185−2199.
(67) de Jongh, L. J.; Miedema, A. R. Experiments on simple magnetic model systems. *Adv. Phys.* **1974**, *23*, 1−260.
(68) Kawasaki, K. Anomalous Spin Relaxation near the Magnetic Transition. *Prog. Theor. Phys.* **1968**, *39*, 285−311.
(69) Kawasaki, K. Ultrasonic attenuation and ESR linewidth near magnetic critical points. *Phys. Lett. A* **1968**, *26*, 543−543.
(70) Mori, H.; Kawasaki, K. Antiferromagnetic Resonance Absorption. *Prog. Theor. Phys.* **1962**, *28*, 971−987.
(71) Huber, D. L. Critical-Point Anomalies in the Electron-Paramagnetic-Resonance Linewidth and in the Zero-Field Relaxation Time of Antiferromagnets. *Phys. Rev. B* **1972**, *6*, 3180−3186.
(72) Kresse, G.; Hafner, J. *Ab initio* molecular dynamics for liquid metals. *Phys. Rev. B: Condens. Matter Mater. Phys.* **1993**, *47*, 558−561.
(73) Kresse, G.; Furthmüller, J. Efficiency of *ab-initio* total energy calculations for metals and semiconductors using a plane-wave basis set. *Comput. Mater. Sci.* **1996**, *6*, 15−60.
(74) Kresse, G.; Furthmüller, J. Efficient iterative schemes for *ab initio* total-energy calculations using a plane-wave basis set. *Phys. Rev. B: Condens. Matter Mater. Phys.* **1996**, *54*, 11169−11186.
(75) Perdew, J. P.; Burke, K.; Ernzerhof, M. Generalized Gradient Approximation Made Simple. *Phys. Rev. Lett.* **1996**, *77*, 3865−3868.
(76) Dudarev, S. L.; Botton, G. A.; Savrasov, S. Y.; Humphreys, C. J.; Sutton, A. P. Electron-energy-loss spectra and the structural stability of nickel oxide: An LSDA+U study. *Phys. Rev. B: Condens. Matter Mater. Phys.* **1998**, *57*, 1505−1509.
(77) Smart, S. J. *Effective Field Theory of Magnetism*; Saunders: Philadelphia, 1966.
(78) Lee, K. H.; Lee, J. Y.; Lee, C.; Whangbo, M.-H. Evaluating the Curie-Weiss Temperature of a Magnetic System Composed of Nonequivalent Magnetic Ions in Terms of Spin Exchange Constants. *Bull. Korean Chem. Soc.* **2014**, *35*, 1277−1278.
(79) Dai, D.; Whangbo, M.-H. Classical spin and quantum-mechanical descriptions of geometric spin frustration. *J. Chem. Phys.* **2004**, *121*, 672−680.

DOI: 10.1021/acs.inorgchem.7b02130
Inorg. Chem. 2017, 56, 14023−14039